Global and Planetary Change 262 (2026) 105424

Contents lists available at ScienceDirect

Global and Planetary Change

journal homepage: www.elsevier.com/locate/gloplacha

Research Article

Enhanced silicate chemical weathering of the South African Plateau and its contribution to the global climate cooling trend during the late cretaceous

Camilo E. Gaitan [a,b], Emmanuelle Pucéat [b,*], Pierre Pellenard [b], Emmanuelle Vennin [b], Fabrice Monna [c], Germain Bayon [d], Thierry Adatte [e], Cécile Robin [f], François Guillocheau [f]

[a] Climerock, Gif-sur-Yvette, France
[b] Université Bourgogne Europe, CNRS, Biogéosciences UMR 6282, 21000 Dijon, France
[c] Université Bourgogne Europe, CNRS, ARTEHIS, UMR, CNRS, 6298, 21000 Dijon, France
[d] Unité de Recherche Géosciences Marines, IFREMER, Plouzané, France.
[e] ISTE, Université de Lausanne 1, Lausanne, Switzerland
[f] Géosciences Rennes, Université de Rennes 1, UMR CNRS, 6118 Rennes, France.

ARTICLE INFO

Editor: Dr. Alan Haywood

Keywords:
Isotope geochemistry
Tectonics-climate
Silicate weathering
South African Plateau
Cretaceous cooling
Marine productivity

ABSTRACT

Climate cooling during the late Cretaceous (ca. 100–66 Ma) has been linked to CO_2 drawdown produced by enhanced denudation episodes recorded in the eastern margin of South America and western margin of South Africa. However, the onset of these episodes is recorded during rather than prior to the main climate cooling stage of the late Cretaceous, reported within the Santonian-Early Campanian interval (about 86–81 Ma). Here, we investigate the clay fraction (<2 μm) of sediments from the borehole O-A1 located in the continental slope of the Cape Basin, adjacent to the western South African Margin. We combine these results with previous records from the basin (DSDP 361) to investigate the controlling factors of the denudation record along the South African Plateau, and their relationship with the climate cooling during the late Cretaceous. The $\Delta\varepsilon_{Hf}$ record (proxy for silicate weathering intensity) from site O-A1 shows an increase in silicate chemical weathering intensity during the Cenomanian-Maastrichtian (ca. 95–68 Ma) interval, predating the Campanian-Danian interval shown by the DSDP 361 record. While this offset between the sites is attributed to age model uncertainties from the site DSDP 361, the observed increase in silicate chemical weathering intensity is concomitant to an enhanced phase of physical erosion and tectonic uplift of the South African Plateau and mirrors the evolution of seawater $^{87}Sr/^{86}Sr$ at that time. Additionally, the duration of this increase even during global climate cooling suggests that the increase in weathering intensity and rate are mainly tectonically driven. Our $\Delta\varepsilon_{Hf}(80)$ data from site O-A1 shows for the first time an increase in silicate chemical weathering intensity as early as the Cenomanian, suggesting not only that it could have played a role in maintaining the cool global climate trend during the late Cretaceous, but that this episode could have contributed to trigger the CO_2 drawdown responsible for the observed cooling record that started by the end of the Turonian in some high-mid latitude locations and extended up to the Campanian. This process appears to be driven by two different mechanisms. First, via silicate reactions, and second through increased nutrient riverine input into the basin, which could have contributed to enhanced primary productivity and organic carbon storage as shown by the increase in Ba_{excess} during the Santonian-Maastrichtian interval (ca. 85–65 Ma). Our study establishes enhanced weathering along the South African Plateau as a potential early contributor to the late Cretaceous cooling trend and highlights the importance of nutrient driven marine productivity as an understudied but potentially significant mechanism for CO_2 drawdown.

1. Introduction

Sedimentary basins represent the best archive to track the long-term evolution of denudation processes in ancient environments. Recent studies conducted in basins adjacent to the eastern South American margin and the western South African margin relate tectonic activity with enhanced denudation episodes, subsequent CO_2 drawdown, and climate cooling (Corentin et al., 2024; 2022, 2023; Gaitan et al., 2023).

* Corresponding author.
E-mail address: emmanuelle.puceat@ube.fr (E. Pucéat).

https://doi.org/10.1016/j.gloplacha.2026.105424
Received 8 April 2025; Received in revised form 25 February 2026; Accepted 6 March 2026
Available online 23 March 2026

These studies have shown through clay mineralogy and isotopic records (Hf-Nd isotopes on clays) an intensification of silicate chemical weathering during the late Cretaceous, an important mechanism for CO_2 drawdown (Berner et al., 1983; Gaillardet et al., 1999; Hilton and West, 2020). These weathering episodes have been associated with the long-term climate cooling trend observed in the late Cretaceous (Friedrich et al., 2012; O'Brien et al., 2017), Hf-Nd isotopic records reveal silicate weathering intensification within the Santonian-Campanian interval in the South American margin (Corentin et al., 2022, 2023), and within the Santonian-Maastrichtian interval in the western South African margin (Corentin et al., 2024; Gaitan et al., 2023). Yet these episodes both coincide with the main cooling phase of the late Cretaceous climatic decline, but begin after its onset, reported earlier in different regions (Friedrich et al., 2012; O'Brien et al., 2017; Petrizzo et al., 2022). In the context of the South African Margin, the proposed increase in chemical weathering intensity relies only on the geochemical record from DSDP core 361. Yet this site presents relatively large uncertainties in the age model of the studied sediments (Gaitan et al., 2023), hindering the identification of a precise timing for the onset of the enhanced weathering episode. Additionally, no major changes in chemical weathering along the South African margin are detected at DSDP core 361 during the Turonian-Campanian interval, which includes the main cooling phase reported by global isotopic records during the late Cretaceous ($\delta^{18}O$ benthic) (Friedrich et al., 2012; O'Brien et al., 2017; Huber et al., 2018; Petrizzo et al., 2022). Therefore, although the recorded weathering episodes along the eastern South American and western South African margins may have contributed to sustain cooling conditions during the late Cretaceous, the mechanisms responsible for the cooling onset remain elusive.

The evolution of the chemical weathering signal from DSDP core 361 relies on the analysis of detrital clay minerals coming predominantly from the South African Plateau and depositing in the abyssal plain of the Cape Basin (Gaitan et al., 2023). However, due to the distal location of the sedimentary record, the incorporation of allogenic sediments by deep-bottom currents is not entirely discarded (Murphy and Thomas, 2013; Natland, 1978), and differential settling processes on clay minerals might also be involved introducing some bias into the paleoclimatic interpretation (Gibbs, 1977; Petschick et al., 1996). Multiple thermochronological data — Apatite-Fission Track (AFT) and Apatite (U-Th)/He (AHe) — have shown that regional structures across the Plateau are important in the rock cooling events during the late Cretaceous (Green et al., 2017; Kounov et al., 2009, 2013; Raab et al., 2002; Stanley and Flowers, 2020; Tinker et al., 2008; Wildman et al., 2015, 2021). These regional structures could have modified the source areas of the denudation episodes (i.e., erosion and weathering) inferred from these rock cooling events. These denudation episodes have been further linked to tectonic uplift involving continental tilting (Baby et al., 2018a, 2019; Braun et al., 2014; Stanley et al., 2021), responsible for drainage reorganization (De Wit et al., 2009; De Wit, 1999; Goudie, 2005; Stevenson and Mcmillan, 2004), and by extension for variations in the sediments source areas. Estimations of sediment fluxes and volumes have also shown that the tilting component of the uplift appears to have affected the sediment distribution along the basins located adjacent to the eastern South African margin (Baby et al., 2019). Altogether, these processes affecting the source and distribution of the sediments deposited in the Cape Basin could have impacted the denudation record, particularly the chemical weathering, and hinder any interpretation of the impact of these processes in the climate during the late Cretaceous. For this reason, a process-response comparison of the denudation record along the Cape Basin appears of prime importance to understand the dynamics controlling this record and the implications for climatic interpretations.

The aim of this study is to investigate the sedimentary record at the continental slope of the Cape Basin (borehole O-A1— Fig. 1) and compare it with previous records from the abyssal plain (DSDP core 361— Fig. 1; Gaitan et al., 2023). Through this comparison we study the impacts of changes in sediment distribution and sources in the erosional and chemical weathering signals recorded along the Cape Basin, also exploring the links of this record to the global climate cooling during the late Cretaceous. To do so, we combine X-ray diffraction (XRD) analyses, major and trace elements, Transmission Electron Microscopy (TEM), and Hf – Nd isotopic compositions on clay fractions (< 2 μm - Bayon et al., 2016). Through this suite of techniques, we seek to understand the dynamics affecting geochemical signals, specifically on the clay fraction across the sediment routing system.

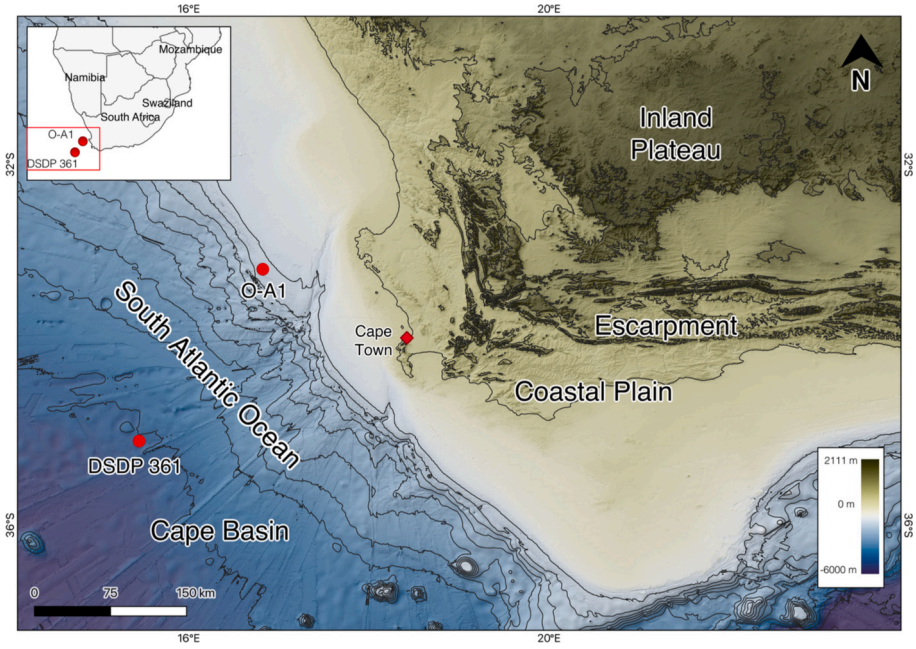

Fig. 1. Map of the source-to-sink system composed by the South African plateau and the Cape basin. O-A1 borehole (33.161539°S; 16.822406°E) is located at the continental slope of the Cape Basin. DSDP core 361 is located in the abyssal plain of the basin (35.066167°S; 15.448500°E). Topography and bathymetry data compiled from NASA JPL, (2013).

2. Geological setting

2.1. Evolution of the southwestern African margin

The South African margin evolution began with the rifting between the South American and African Plates and the subsequent opening of the Atlantic Ocean during the late Jurassic – early Cretaceous (Moulin et al., 2010; Torsvik et al., 2009). It has been suggested that this opening started at the southern segment and moved northwards (Koopmann et al., 2016; Rabinowitz and LaBrecque, 1979), but the rifting onset in the southern segment is not yet fully understood due to age uncertainties on the magnetic anomalies (e.g., Baby et al., 2018b; Moulin et al., 2010). However, it is acknowledged that magnetic anomaly M3 at 130 Ma marks the rifting-drifting transition in this segment (Collier et al., 2017). Deposition during this period was marked by large volcanic activity linked to the Paraná-Etendeka Large Igneous Province (ca. 135–133 Ma; Gomes and Vasconcelos, 2021; Renne, 2015), this is supported by the presence of Seaward-Dipping Reflectors (SDRs) overlying graben and half graben basement structures (Gladczenko et al., 1997). Regional Valanginian-Hauterivian fault-bounded *syn*-rift sequences developed across the southwestern African basins (Séranne and Anka, 2005). These sequences comprised lava flows with continental sediments, essentially sandstones and claystones (Hirsch et al., 2010; Jungslager, 1999; Van Der Spuy, 2003).

Post-rift deposits of about 3 to 5 km of thick siliciclastic sequences were deposited and distributed along the 4 basins adjacent to the margin: Walvis, Lüderitz, Orange, and Cape (Aizawa et al., 2000). Baby et al. (2018b) defined three main first-order depositional phases for these post-rift deposits. The first phase was a retrogradational stage (131–93.5 Ma) marked by an increased rate of accommodation space compared to sediment supply. The creation of this accommodation space was associated with the thermal subsidence of the margin. During the second stage (93.5–66 Ma), deposition shifted to a predominant progradational-aggradational phase, while the margin was tilted seawards (Aizawa et al., 2000; Baby et al., 2019). A pronounced increase in sediment supply related to the tectonic uplift of the South African Plateau is linked to this depositional change. The final stage (66–0 Ma) comprised primarily a retrogradational phase, although there was a progradational stage within this period at ca. 27 Ma (Baby et al., 2018b). The retrogradational stage was likely associated with the stabilization of the inland Plateau and climate aridification, which led to a decrease in sediment supply.

The stratigraphy of the margin is divided in 8 units bounded by stratigraphic markers (e.g., unconformities or maximum flooding surfaces) that define relevant regional deposition cycles (Baby et al., 2019; Baby et al., 2018b). Lithology of these post-rifting units comprises mainly siltstones, although limestones are also an important component in the Unit 1 (130–113 Ma) from the Walvis and Lüderitz basins (Baby et al., 2019).

2.2. Cape basin

The Cape Basin is divided in 8 units and bounded by the regional stratigraphic surfaces defined in the basins along the margin. The Cretaceous interval in the basin spans between Unit 1 and 5 (Baby et al., 2018b). Unit 1 is bounded by the unconformities 6At1 (130 Ma) and 13At1 (113 Ma), the former representing the breakup unconformity and the latter a depositional hiatus (Paton et al., 2008; Paton et al., 2007). This unit comprises a sedimentary package evidencing the rifting-drifting transition of the margin. At the base, aeolian sandstones with basalts are covered by carbonate cemented marine sandstones. On top, shelly sandstones with some local lagoonal limestones are topped by marine shales (Baby et al., 2018b). The upper boundary of Unit 2 is the seismic marker 14At1 (100 Ma). This unit is dominated by silty-claystones overlain by shales that define marker 14At1 (Baby et al., 2018b). This unit comprises a predominant retrogradational trend (Baby et al., 2019), but most importantly evidences sediment supply from two disconnected deltaic systems located south of the modern Orange river system (Baby et al., 2018b). Unit 3 consists entirely of deep marine shales (Baby et al., 2018b; Paton et al., 2008), with marker 15At1 (93.5 Ma) as the upper boundary. The depositional trend in this unit is mostly retrogradational, marked by wedges backstepping (Baby et al., 2019). The upper boundary of Unit 4 is marked by the unconformity 17At1 (81 Ma), which has been interpreted as a major sea-level fall. Claystones dominate in this unit in a predominantly aggradational depositional trend. The top of Unit 5 is marker 22At1 at the Maastrichtian-Paleogene boundary (66 Ma). The depositional trend changes from aggradational to progradational, linked to variations in the ratio of subsidence and sediment supply (Baby et al., 2018b; de Vera et al., 2010). Lithology in this unit is dominated by clayey siltstones (Baby et al., 2018b). Unit 6 lies on top of the Cretaceous sequence and it is bounded on top by an Oligocene unconformity (Baby et al., 2018b; de Vera et al., 2010). This unit displays deltaic progradational units (Baby et al., 2018b; de Vera et al., 2010).

3. Material and methods

3.1. Borehole description

In this study we analysed 91 cutting samples from the borehole O-A1 provided by the South African Petroleum Agency. This borehole is located at the continental slope of the Cape Basin (Fig. 1; 33.161539°S 16.822406°E), around 100 km off the southwestern African margin. The borehole comprises a stratigraphic succession of about 3650 m, spanning from the Aptian - Barremian to the middle Eocene period (Valicenti et al., 1993), but the samples analysed in this study span between the Albian and Ypresian periods (i.e., 115–55 Ma), representing Unit 1 to 5 from those described by Baby et al. (2019) (Fig. 2). The basement of the borehole consists of volcanic rocks presumably Hauterivian in age (ca. 132 Ma; Valicenti et al., 1993). On top, there is an Aptian-Albian sequence of argillaceous sandstones (ca. 125–100 Ma), with increased clay abundance at the top and the base. At the late-early Cretaceous boundary (100 Ma), the predominant lithology are claystones interbedded with sandstone layers (Dudus et al., 1992), some minor dolomite stringers are also present in this interval. Throughout the late Cretaceous (100–66 Ma) the succession consists of claystones with occasional pyrite, and stringers of limestones, dolomites, and siltstones (Dudus et al., 1992). Siltstones stringers are predominantly argillaceous and glauconitic. The interval between the Paleocene and the middle Eocene (ca. 66–50 Ma) consists of claystones with sporadic fossiliferous limestones and siltstone stringers (Dudus et al., 1992). At the base of this interval, stringers are scarce and claystones are more calcareous, dolomite stringers are present as well. Sporadic pyrite and glauconite occur within the claystones along the whole interval (Dudus et al., 1992).

The selected samples were targeted considering even distribution within the studied time interval (i.e., 115–55 Ma) and clay content. To ensure an even distribution of the analysed samples, an age model (Supplementary material FS1) was built based on the planktonic foraminifera report by Valicenti et al. (1993).

There were no elements to determine either the Aptian-Albian boundary (113 Ma) or the Albian stage (113–100.5 Ma), which could be missing. Only the occurrence of *Globuligerina hoterivica* around 4170 mbsf indicated late Aptian ages, so the Aptian-Albian boundary was tentatively placed at this depth (113 Ma). A late Albian-Mid Cenomanian (ca. 105–97 Ma) interval was defined around 3624 mbsf based on the last occurrence of *Rotalipora appenninic*a. The Cenomanian-Turonian boundary (93.9 Ma) was placed at 3570 mbsf based on the appearance of *Helvetoglobotruncana helveti*ca. The last occurrence of this assemblage indicated a Mid-Turonian age (ca. 91 Ma) at 3408 mbsf, but there were no elements to define the Turonian-Coniacian boundary (89.8 Ma). An increase in the occurrence of *Marginotruncana coronata* and the appearance of *Globotruncana species* enabled to place an interval

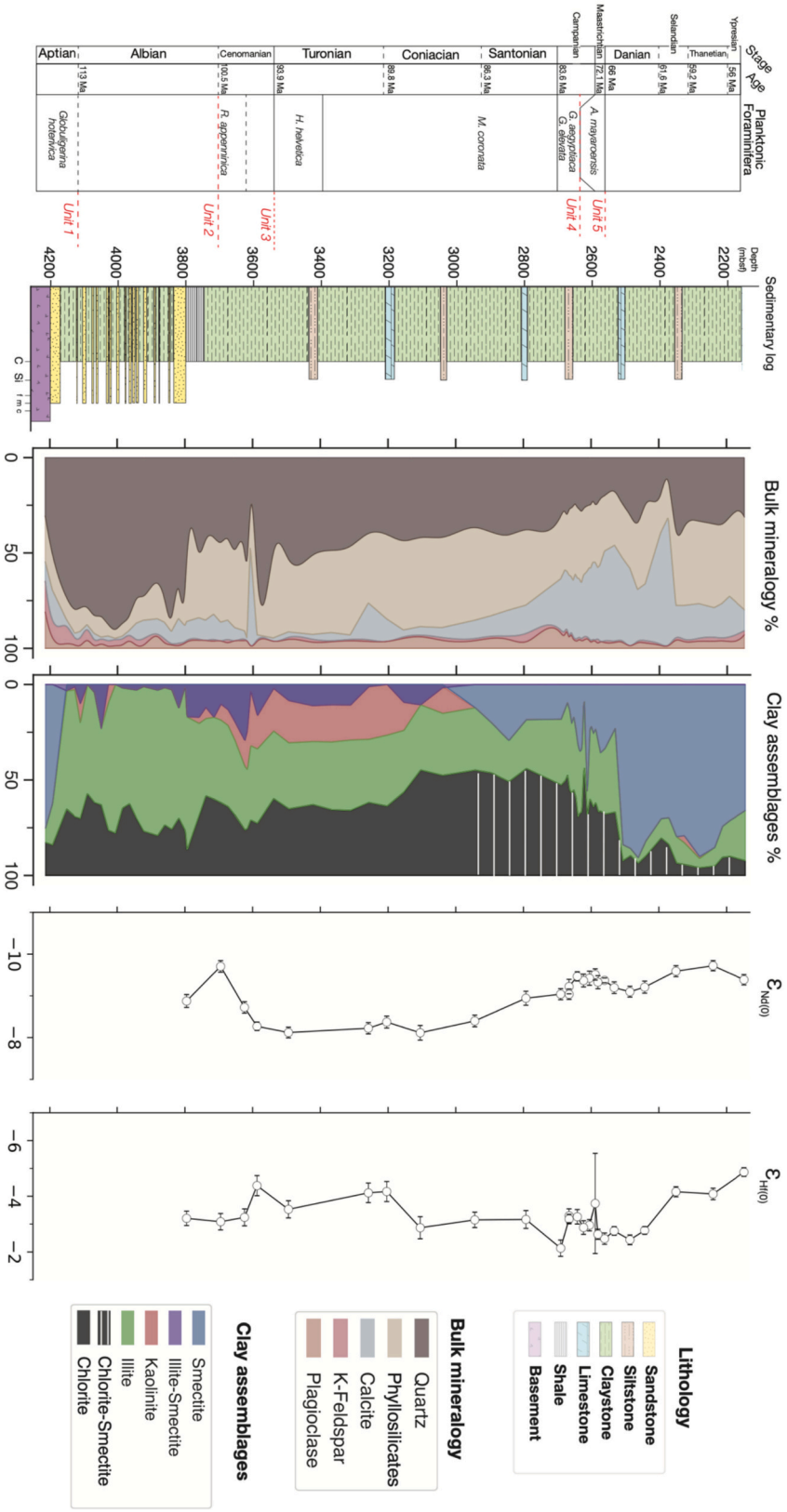

Fig. 2. Biostratigraphy (planktonic foraminifera), sedimentary log, bulk mineralogy, clay assemblages, and present-day ε_{Nd} - ε_{Hf} isotope compositions of the analysed samples from borehole O-A1. Units refer to the classification established by Baby et al. (2019). Planktonic foraminifera abbreviations: R. appenninica = Rotalipora appenninica; H. helvetica = Helvetoglobotruncana helvetica; *M. coronata* = Marginotruncana coronata; *G. elevata* = Globotruncanita elevata; *G. aegyptiaca* = Globotruncanita aegyptiaca; A. mayaroensis = Abathomphalus mayaroensis. Error bars represent the standard deviation (2 μm) calculated for both ε_{Nd} and ε_{Hf}. Both ε_{Nd} and ε_{Hf} isotopic values are reported for $t = 0$.

Coniacian-Santonian (89.8–83.6 Ma) around 2706–2751 mbsf, but the boundary cannot be determined with certainty. Following the occurrence of *Globotruncanita elevata*, distinctive of Campanian age, the Santonian-Campanian boundary (83.6 Ma) was placed at 2697 mbsf. The occurrence of *Globotruncanita aegyptiaca* indicative of a late Campanian age (ca. 75 Ma) and the last occurrence of *Globotruncana ventricosa* enabled to place the Campanian-Maastrichtian boundary (72.1 Ma) around 2580 mbsf. The presence of *Abathomphalus mayaroensis* around 2553 mbsf is indicative of a late Maastrichtian age. No characteristic Danian fauna was identified. The *Globanomalina chapmani* characteristic of a Selandian-Thanetian age was observed around the interval 1550–1340 mbsf, however it was joined by species like *Globigerinatheka index*, which is characteristic of Eocene (ca. 40 Ma). The Maastrichtian-Danian boundary (66 Ma) was then placed at 2553 mbsf, and the subsequent Cenozoic upper interval was tied to an Eocene age (33.9 Ma) around 1340 mbsf.

Based on these planktonic foraminifera fossil assemblages, intervals and age boundaries were established following the ICS chronostratigraphic chart v2023/06 (Cohen et al., 2013; Updated 2023). The age model was built using linear regressions between seven tie-points: the Aptian-Albian boundary (113 Ma; 4170 mbsf), the Mid-Cenomanian (97.2 Ma; 3624 mbsf), the Cenomanian-Turonian boundary (93.9 Ma; 3570 mbsf), the Santonian-Campanian boundary (83.6 Ma; 2697 mbsf), the Campanian-Maastrichtian boundary (72.1 Ma; 2580 mbsf), The Maastrichtian-Danian (66 Ma; 2553), and the Eocene stage tentatively at 1340 mbsf (ca. 34 Ma).

3.2. Analytical techniques

3.2.1. X-ray diffraction (XRD) analyses

XRD analyses were performed for 77 samples for both bulk rock and clay fractions (< 2 μm) in the Biogéosciences Laboratory (UMR CNRS 6282) at the University of Burgundy, France (Supplementary table S1). The bulk rock samples were grounded and set in disks adapters while the clay fractions were prepared as oriented glass slides. Both set of measurements were performed on a Bruker D8 Endeavor diffractometer with Cu-Kα radiations, a LynxEye detector coupled to a Ni filter, and under 40-kV voltage with 25-mA intensity. For the clay fraction (< 2 μm), each oriented glass slide was measured three times following the protocol set by Moore and Reynolds (1989), including both ethylene glycol and heating (490 °C) preparation stages. The main intensity peaks were identified using the MacDiff software 4.2.5 (Petschick, 2001), and the mineral proportions, both for bulk and clay fractions, were determined by calculating the area under the basal reflections peaks (d001). For the clay fractions (< 2 μm) this calculation was done using the resulting diffractograms from the ethylene glycol treatment (Moore and Reynolds, 1989).

3.2.2. Transmission Electron Microscopy (TEM) observations

TEM analyses were performed on clay fractions from 6 samples (Supplementary table S1) at the Agroécologie Institut from the Institut National de Recherche pour l'agriculture, l'alimentation et l'environnement (INRAE) at the University of Burgundy, France. The samples were dispersed in distilled water and 2% *v*/v butylamine solution and then set on a carbon formvar Cu grid. Images were taken using a MET Hitachi 4800.

3.2.3. X-ray fluorescence (XRF) analyses

Forty samples were processed for major and minor oxides abundances (Supplementary table S1) using XRF at the Institut Sciences de la Terre, at the University of Lausanne, Switzerland. Fused disks were prepared from 1.2 g calcined sample powder mixed with Lithium-Tetraborate (1:5 proportions). The measurements were done using a wavelength dispersive PANalytical Axios^{mAX} spectrometer fitted with a 4 kW Rh X-ray tube. Rock silicate reference materials were used for calibration.

3.2.4. Chemical processing for trace element and isotopic analyses

Twenty four samples were grounded and processed (1.3 to 1.5 g of powder) through sequential leaching following a procedure based on the protocols described in Bayon et al. (2002) and Gutjahr et al., (2007—(Supplementary table S1). Carbonates were first removed using 10% v/v acetic acid reacting overnight with the samples. After a rinsing stage with ultrapure 18.2 MΩ water, the Fe-Mn oxyhydroxide phases were removed using a 0.5 M hydroxylamine hydrochloride solution in 20% v/v acetic acid reacting with the samples for 48 h. After another rinsing stage with ultrapure 18.2 MΩ water, organic matter was removed using a 5% H_2O_2 solution reacting with the samples for 48 h, to finally be rinsed again with ultrapure 18.2 MΩ water. Clay fractions (< 2 μm) were separated after this leaching sequence using particle decantation according to the Stokes law.

After leaching and sampling of the clay fraction (< 2 μm) the samples were dried and processed by alkaline fusion following the protocol described in Bayon et al., 2009. Three 3 certified reference standards (BHVO-2, MAG-1, and BCR-2) from the United States Geological Survey (USGS) were also included during the alkaline fusion. Around 50 mg of each sample were placed into carbon crucibles together with 0.6 g of NaOH, 1.2 g of Na_2O_2, and 0.5 g of Tm spike. The crucibles underwent a heating stage at 650 °C during 12 min in a furnace, to then be cooled down with ultrapure 18.2 MΩ water, resulting in the precipitation of Fe-hydroxides. The samples were then centrifuged, and finally dissolved in 3,3 ml of 6 M HCl. From this solution, 0.3 ml were extracted for trace elements analyses. The Tm spike was added as an internal standard in the quantification of trace elements following the method described in Barrat et al. (1996).

3.2.4.1. Trace elements. Trace element concentrations were measured by inductively coupled plasma mass spectrometry (ICP-MS) on a Thermo Scientific X-Series II®, at the Pole Spectrométrie Océan in Brest, France (Supplementary table S2). We used standard bracketing with the Tm spike to quantify trace elements as described in Barrat et al. (1996) and Freslon et al. (2011). Accuracy control and reproducibility were assessed analysing the 3 USGS reference standards: BHVO-2, MAG-1, and BCR-2 (Supplementary table S3). Deviations of trace elements from the reference BHVO-2 (Jochum et al., 2016) were below 14%. For MAG-1 and BCR-2 standards, some elements presented higher deviations, in particular the light rare earth elements (LREE) at around 20% (Supplementary table S3).

3.2.4.2. Hf-Nd Isotopic analyses. Extraction of Hf and Nd for 24 samples was performed by ion chromatography using singled customed columns with AG50W-X8 (200–400 mesh) resin for REE + Hf, Ln Spec resin (50–100 μm) for the Nd fraction, and Ln Spec resin (100–150 μm) for the Hf fraction. Column chromatography was performed applying the adapted separation protocol for Hf and Nd described in Gaitan et al. (2023) for the low pressure, automated column chromatography, PrepFAST-MC® system device. Isotopic measurements were performed using a MC-ICP-MS Neptune Plus® (ThermoFisher-Scientific) at the École Normale Supérieure (ENS) of Lyon, France. Errors are reported as 2 standard deviations (2 sd).

Hafnium isotope measurements performed at the ENS consisted of a static acquisition method of 40 cycles, with an average intensity of 4.3 V throughout the session. Ratios were corrected for mass bias through exponential law and using the stable isotope ratio $^{176}Hf/^{177}Hf = 0.7235$. Mass bias corrected $^{176}Hf/^{177}Hf$ ratios were normalized to a JMC 475 value of 0.282163 (Blichert-Toft et al., 1997). Repeated measurements of bracketed JMC 475 standards during the analytical session gave a ratio of $^{176}Hf/^{177}Hf = 0.282270 \pm 0.000006$ (21 ppm, $n = 17$). Reference standards BHVO-2 and BCR-2 gave $^{176}Hf/^{177}Hf$ normalized isotopic values of 0.283103 ± 0.000020 (70 ppm, $n = 3$) and 0.282869 ± 0.000004 (14 ppm, $n = 1$) respectively. Both standards were within the range of reference values determined by Weis et al. (2005). Four

procedural blanks for Hf were also measured, obtaining values between 27 and 44 pg (Supplementary table S3).

Neodymium isotope measurements performed at the ENS consisted of a static acquisition method of 40 cycles, with an average intensity of 5 V. Ratios were corrected for mass bias through exponential law and using the stable isotope ratio $^{143}Nd/^{144}Nd = 0.7219$. Mass bias corrected $^{143}Nd/^{144}Nd$ ratios were normalized to a JNdi-1 value of 0.512115 (Tanaka et al., 2000). Repeated measurements of bracketed JNdi-1 standards during the analytical session gave a ratio $^{143}Nd/^{144}Nd = 0.511980 \pm 0.000009$ (18 ppm, $n = 16$). Reference standards BHVO-2 and BCR-2 gave $^{143}Nd/^{144}Nd$ normalized isotopic values of 0.512984 ± 0.000013 (25 ppm, n = 3) and 0.512644 ± 0.000009 (17 ppm, $n = 2$) respectively. Both standards were consistent with the reference values determined by Weis et al. (2005). Four procedural blanks for Nd were measured as well, obtaining values between 18 and 313 pg, which are approximately 1 × 103 times lower than the average concentrations obtained for the samples (Supplementary table S3).

Results for hafnium and neodymium isotopic compositions are reported in epsilon notation relative to the deviation from the chondritic reference material (CHUR) reported in Bouvier et al., 2008, $^{176}Hf/^{177}Hf_{CHUR} = 0.282785$ and $^{143}Nd/^{144}Nd_{CHUR} = 0.512630$:

$$\varepsilon_{Hf} = \left(\left[\frac{\left(\frac{176Hf}{177Hf}\right)_{Sample}}{\left(\frac{176Hf}{177Hf}\right)_{CHUR}} - 1 \right] * 10^4 \right) \quad \text{and } \varepsilon_{Nd} = \left(\left[\frac{\left(\frac{143Nd}{144Nd}\right)_{Sample}}{\left(\frac{143Nd}{144Nd}\right)_{CHUR}} - 1 \right] * 10^4 \right)$$

ε_{Nd} and ε_{Hf} values are also reported age corrected (t = 80 Ma; Table 1). The ε_{Hf} values were corrected for radioactive decay of ^{176}Lu to ^{177}Hf using the measured Lu and Hf concentrations ($^{176}Lu/^{177}Hf = Lu/Hf * 0.1419$), the ^{176}Lu radioactive decay constant λ (1.867 ± 0.008 × 10–11 year-1; Söderlund et al., 2004), and the present-day $^{176}Lu/^{177}Hf_{(CHUR)}$ value of 0.336 (Bouvier et al., 2008). The ε_{Nd} values were corrected for radioactive decay of ^{147}Sm to ^{144}Nd using the measured Sm and Nd concentrations ($^{147}Sm/^{144}Nd = Sm/Nd * 0.6049$), the ^{147}Sm radioactive decay constant λ (6.54×10^{-12} year^{-1}; Lugmair and Marti, 1977), and the present-day $^{147}Sm/^{146}Nd_{(CHUR)}$ value of 0.1960 (Bouvier et al., 2008).

Calculations of the epsilon values and $\Delta\varepsilon_{Hf}$ were done at 80 Ma to interpret the data. This is the age used for the data from site DSDP 361 to compare with the source units from the South African Plateau due to the significant uncertainties in the age model of the site (Gaitan et al., 2023). This age represents approximately the midpoint of the analysed time interval.

ε_{Nd} and ε_{Hf} values from clay fractions display a correlation that is denominated as the "Clay Array" (Bayon et al., 2016). Offsets in ε_{Hf} values from this array are expressed as ΔεHf (Eq. 1) and account for the intensity in chemical weathering (Bayon et al., 2016). $\Delta\varepsilon_{Hf}$ values were calculated using ε_{Nd} and ε_{Hf} values at present time (t = 0) and age-corrected to 80 Ma, these values are reported in Table 1. Calculations of the epsilon values and $\Delta\varepsilon_{Hf}$ were done at 80 Ma to interpret the data. This is the age used for the data from site DSDP 361 to compare with the source units from the South African Plateau due to the significant uncertainties in the age model of the site (Gaitan et al., 2023). This age represents approximately the midpoint of the analysed time interval.

$$\Delta\varepsilon_{Hf}(t) = \varepsilon_{Hf}(t) - (0.78^{*}\,\varepsilon_{Nd}(t) + 5.23) \quad (1)$$

4. Results

4.1. Bulk rock composition and clay mineral assemblages – XRD analyses

Bulk rock composition measured shows a predominance of quartz and phyllosilicates (i.e., clays and micas) along the section, with calcite only becoming predominant after the Santonian (~2800 mbsf; ca. 84 Ma) (Supplementary table S4; Fig. 2). At the base, during the Aptian-Albian interval (ca. 114–110 Ma), quartz content increases reaching values around 88%. Above, quartz content decreases while phyllosilicates content increases, reaching values up to 35% in the Turonian (ca. 90 Ma). An increase in calcite concentrations is observed at the

Table 1
Hf-Nd isotopic compositions. Depth interval represents the range from where the sample was taken. Reported depth is the depth used to calculate the sample age and plot the data in Fig. 2. Depth and depth interval are reported in meters below the sea floor (mbsf). *Ages were calculated using an age model built from the biostratigraphy report by Valicenti et al. (1993). Error accounts for the standard error. $\Delta\varepsilon_{Hf}$ was calculated using the clay array correlation: $\Delta\varepsilon_{Hf} = \varepsilon_{Hf} - (0.78 * \varepsilon_{Nd} + 5.23)$ published in Bayon et al. (2016). 2σ is the standard deviation calculated for both ε_{Nd} and ε_{Hf}.

Sample	Depth interval (mbsf)	Depth (mbsf)	Age (Ma)*	$^{143}Nd/^{144}Nd$	ε_{Nd}	2σ	$^{176}Hf/^{177}Hf$	ε_{Hf}	2σ	$\varepsilon_{Nd(80)}$	$\varepsilon_{Hf(80)}$	$\Delta\varepsilon_{Hf(80)}$
O-A1/1	2145–50	2147	55	0.512149	−9.39	0.12	0.282647	−4.87	0.16	−8.45	−3.60	−2.24
O-A1/5	2235–45	2240	57	0.512132	−9.72	0.12	0.28267	−4.08	0.21	−8.76	−2.87	−1.27
O-A1/10	2346–55	2349	60	0.512138	−9.59	0.13	0.282667	−4.16	0.18	−8.66	−2.97	−1.45
O-A1/14	2439–45	2442	63	0.512158	−9.21	0.14	0.282707	−2.77	0.14	−8.36	−1.59	−0.30
O-A1/16	2481–90	2485	64	0.512164	−9.1	0.13	0.282716	−2.44	0.18	−8.17	−1.29	−0.15
O-A1/18	2529–35	2532	65	0.512159	−9.19	0.14	0.282707	−2.75	0.15	−8.30	−1.63	−0.39
O-A1/21	2562–71	2560	67	0.51215	−9.37	0.06	0.282715	−2.48	0.2	−8.47	−1.36	0.01
O-A1/23	2577–83	2580	72	0.512152	−9.33	0.16	0.282711	−2.63	0.18	−8.44	−1.49	−0.13
O-A1/24	2583–92	2588	73	0.512142	−9.51	0.14	0.282679	−3.74	1.8	−8.64	−2.62	−1.11
O-A1/27	2604–07	2605	74	0.512147	−9.42	0.17	0.282701	−2.96	0.2	−8.52	−1.86	−0.44
O-A1/30	2619–25	2622	76	0.51215	−9.37	0.15	0.282704	−2.88	0.24	−8.46	−1.73	−0.36
O-A1/33	2637–43	2640	78	0.512145	−9.47	0.11	0.282693	−3.26	0.26	−8.55	−2.16	−0.72
O-A1/37	2661–67	2665	80	0.512157	−9.22	0.17	0.282692	−3.3	0.25	−8.23	−2.09	−0.90
O-A1/37 (2)	2661–67	2665	80	0.512167	−9.04	0.12	0.282695	−3.18	0.17	−8.23	−2.09	−0.90
O-A1/40	2685–94	2690	83	0.512167	−9.04	0.13	0.282725	−2.14	0.29	−8.13	−1.01	0.11
O-A1/43	2790–96	2792	85	0.512172	−8.94	0.17	0.282695	−3.17	0.32	−7.98	−2.12	−1.12
O-A1/46	2943–46	2944	86	0.5122	−8.4	0.14	0.282696	−3.15	0.28	−7.42	−2.13	−1.57
O-A1/49	3102–08	3105	88	0.512214	−8.11	0.17	0.282704	−2.87	0.4	−7.14	−1.77	−1.44
O-A1/51	3201–07	3204	89	0.512201	−8.37	0.14	0.282667	−4.17	0.36	−7.45	−3.18	−2.59
O-A1/52	3255–61	3258	90	0.512208	−8.22	0.13	0.282668	−4.12	0.35	−7.32	−3.20	−2.73
O-A1/57	3492–98	3494	93	0.512214	−8.12	0.13	0.282685	−3.53	0.31	−7.14	−2.53	−2.19
O-A1/60	3582–91	3587	95	0.512206	−8.27	0.1	0.282661	−4.38	0.36	−7.31	−3.41	−2.94
O-A1/63	3624–27	3624	97	0.512183	−8.72	0.14	0.282693	−3.24	0.3	−7.73	−2.32	−1.52
O-A1/66	3693–96	3694	99	0.512132	−9.71	0.14	0.282698	−3.09	0.29	−8.63	−2.06	−0.56
O-A1/70	3792–98	3795	102	0.512175	−8.87	0.15	0.282694	−3.21	0.26	−7.84	−2.41	−1.53

Cenomanian (ca. 96 Ma). Since the Coniacian, calcite content increases in parallel with a decrease in quartz content, while phyllosilicates proportions remain stable at values around 35%. The increase in calcite content continues up to the Maastrichtian-Paleogene transition, where it reaches values around 50%. Between the Danian and the Ypresian, quartz and phyllosilicates content increase up to values around 35% and 40%, respectively. Calcite content decreases from the Danian onwards, reaching values close to 20% and only showing a positive excursion around the Danian-Selandian boundary with values close to 55%. Plagioclase and K-Feldspar are present throughout the section but in minor proportions. The percentages along the section are around 8%, except for sample O-A1/−91 at the base of the section with 16% and 19% for K-Feldspar and plagioclase, respectively. Other minerals like pyrite, halite, and gypsum, are also present along the section but in proportions lower than 10% (Supplementary table S4).

The clay assemblages at the base of the section are dominated by smectite with values close to 75% (Supplementary table S4; Fig. 2). However, in the late Aptian (ca. 113 Ma), smectite disappears simultaneously with the appearance of illite-smectite mixed layer, which reaches values around 10%. During the Aptian-Albian interval, illite and chlorite increase to values around 50% and 30%, respectively. By the early Cenomanian (ca. 100 Ma), illite values decrease to around 15%, following an increase in illite-smectite and kaolinite. From the Cenomanian to the Turonian, most of the clay assemblages remain stable, with values around 35% for both chlorite and illite, 15% for kaolinite, and around 10% for illite-smectite. Chlorite displays an increase around the Turonian-Coniacian transition and chlorite-smectite mixed layers start to appear in the late Coniacian (ca. 86 Ma), whereas illite decreases to values around 20%. By late Coniacian (ca. 87 Ma), illite-smectite and kaolinite disappear concomitantly with the appearance of smectite, with illite also showing a decrease to 10%. Since then, smectite increases steadily up to the Danian (ca. 65 Ma) where it peaks at values around 75%. Concomitant with such an increase, chlorite-smectite abundance decreases and reaches values around 25% in the Maastrichtian-Danian transition. Illite oscillates during this period but displays a subtle increase reaching values close to 30% in the Maastrichtian-Danian transition. During the Danian-Ypresian interval, smectite remains the most abundant assemblage with values close to 70%, while illite and chlorite-smectite decrease significantly to values around 8%. However, during the Thanetian, illite shows a continuous increase to values around 20%.

4.2. Hf - Nd isotopic compositions

The measured ε_{Hf} values range between −4.8 and −2.1 ε-units throughout the section (Fig. 2; Table 1). During the Albian, ε_{Hf} values remain stable around −3 ε-units, only to decrease to −4.3 ε-units in the Cenomanian (ca. 95 Ma). Above, values show a slight increasing trend up to the late Santonian (ca. 85 Ma), where they reach values around −2 ε-units. During the early Campanian there is a drop in the values down to −3.7 ε-units, followed by a very minor increasing trend that continues up to the early Danian (ca. 65 Ma), where they reach back to values around −2.5 ε-units. Lastly, the values decrease during the Danian-Ypresian to reach a minimum of −4.9 ε-units. Measured ε_{Nd} values range between −9.7 and − 8.1 ε-units throughout the section (Fig. 2; Table 1). From the Albian up to the early-Coniacian (ca. 89 Ma), ε_{Nd} values display a slight increase from −8.8 to −8.4 ε-units, apart from a negative excursion (−9.7 ε-units) in the late Albian (ca. 102 Ma). Above the Coniacian, the ε_{Nd} values display a long subtle negative trend up to the Thanetian (ca. 58 Ma), where they reach values around −9.7 ε-units. However, in this interval there is a minor increasing period during the Danian, where values show a show a very minor increase from −9.3 to −9.1 (Fig. 2).

4.3. Major and REE elements

Major oxides concentrations are reported in the Supplementary table S5. The SiO_2 wt% is predominant among the samples with percentages between 24% and 82%. Second in abundance are CaO wt%, Fe_2O_3 wt%, and Al_2O_3 wt%, with concentrations reaching up to 28%, 19%, and 15%, respectively. Other major oxides like MgO wt%, K_2O wt%, and Na_2O wt %, are present at percentages lower than 4 wt%, whereas major oxides like TiO_2 wt%, MnO wt%, P_2O_5 wt%, Cr_2O_3 wt%, and NiO wt%, are at percentages lower than 1 wt%.

REE elements for the clay fraction (< 2 μm) are reported together with other trace elements in Supplementary table S2. The REE concentrations for samples below sample O-A1/43 (below 2793 mbsf – 85 Ma) display a flat pattern with a very subtle depletion in HREE over LREE (Fig. 3). In contrast, samples in the upper part of the section (above 2793 mbsf – 85 Ma) show REE patterns with a slight depletion in LREE and MREE. Additionally, these samples show positive Eu anomalies (Eu/Eu* > 1; Supplementary table S2). Such anomalies are likely introduced due to undercorrected isobaric interferences associated with high Ba contents (>2000 ppm; Supplementary table S2) (e.g., Lidman et al., 2019; Zhu and Itoh, 2021), therefore Eu values were removed from the REE plot.

4.4. Transmission electron microscopy

Six samples evenly distributed along the section were analysed through TEM imagery (Fig. 4; Supplementary table S1). At the base of the section (sample O-A1/88; 4151mbsf – 112 Ma) clay particles show rather regular textures with defined edges, specially illite particles that are present as elongated euhedral prisms (Fig. 4A). By the low-middle part of the section (sample O-A1/61; 3607 mbsf – 96 Ma) particle texture shows a rather altered structure, and illite-smectite mixed-layers (I-S R1) start to appear. The texture shows smaller, thinner, elongated and more fibrous particles (Fig. 4B; 'hairy-like' type). Above (sample O-A1/50; 3155 mbsf – 88 Ma), illite-smectite mixed-layers (I-S R1) seem less altered, but still rather long and fibrous (Fig. 4C). Kaolinite also starts to become more frequent, with a characteristic hexagonal regular shaped texture (Fig. 4C). By the upper-middle part of the section (O-A1/32; above 2635 mbsf – 77 Ma), clay particles show predominantly flaky-shape texture, characteristic of smectite particles (Fig. 4D). Thin-elongated particles interpreted as illite also become more frequent (Fig. 4D).

5. Discussion

5.1. Clay minerals origin

Detrital clay minerals deposited in sedimentary basins are useful tracers to understand the evolution of surface continental processes (e.

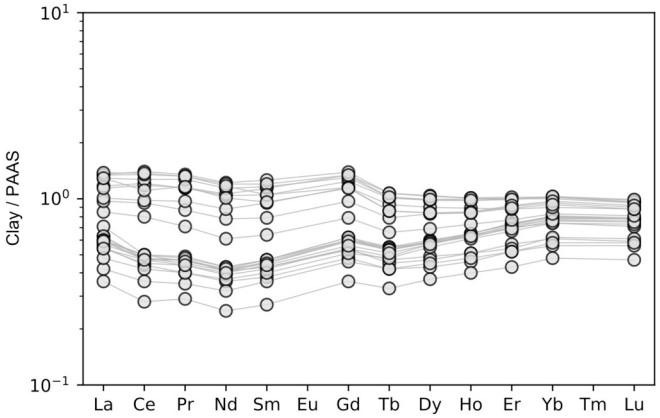

Fig. 3. REE concentrations of the clay fraction (< 2 μm) from borehole O-A1. REE contents were normalized to the Post-Archean average Australian Shale (PAAS; Taylor and McLennan, 1985).

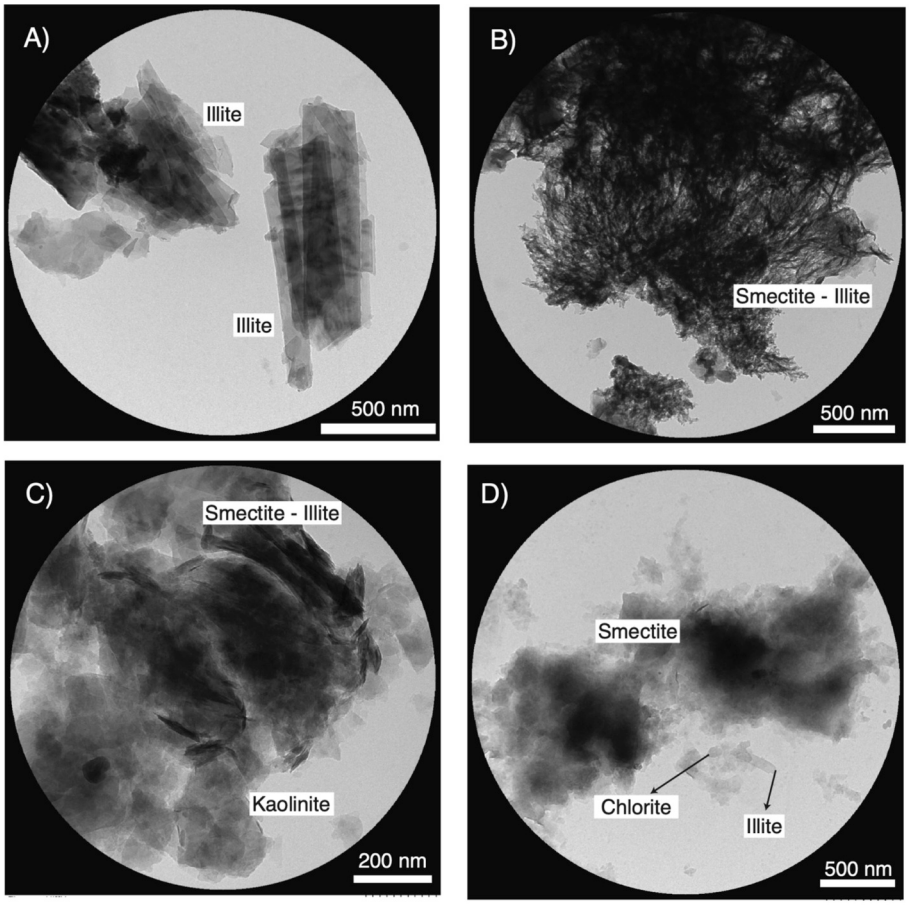

Fig. 4. A) TEM image from sample O-A1/88 exhibiting long elongated regular-shaped illite particles. B) TEM image from sample O-A1/61 showing interlayered illite-smectite highly altered, thin, and fibrous. C) TEM image from sample O-A1/50 showing interlayered illite-smectite, showing an elongated fibrous texture. At the bottom of the image a hexagonal kaolinite particle can be observed as well. D) TEM image from sample O-A1/32 showing smectite particles and regular polygonal illite and chlorite particles.

g., Bougeault et al., 2017; Chamley, 1989; Corentin et al., 2022, 2023; Dera et al., 2009; Gaitan et al., 2023). However, clay minerals can also form within sedimentary basins through processes such as hydrothermal activity, reverse weathering, alteration of volcanic ash falls, or in deep-sea conditions by the interaction between sediments constituents and seawater (Chamley, 1989; Velde, 1995; Warr, 2022). Clay mineral assemblages can also be modified after formation or deposition during burial diagenesis in the basin (Chamley, 1989; Ketzer et al., 2003; Lanson et al., 2002). Therefore, to interpret variations in clay mineral assemblages in terms of surface continental processes, clay minerals at sedimentary basins should be identified first as detrital particles inherited from the landmasses where they were formed and without significant alteration.

The clay record of borehole O-A1 shows from top to bottom a clear and progressive influence of burial diagenesis, which is common for the depths range observed in borehole O-A1 (i.e., $>$ 2500 mbsf; Fig. 2). At the top of the section, smectite predominates with minor presence of illite and chlorite-smectite mixed layers. Smectite disappears progressively with depth, illite-smectite (R1) layers start to appear, and chlorite becomes more abundant in chlorite-smectite mixed layers, until only illite and chlorite are remaining at the base of the section (Fig. 2). This transition in clay assemblages is diagnostic of burial diagenesis. Smectites are the most sensitive clay minerals and start to transform into illite-smectite mixed layers around 70 °C through illitization process, until a full transformation into illite is completed (Chamley, 1989; Lanson et al., 2009; Nadeau et al., 1985; Surdam and Crossey, 1987; Warr, 2022). Illitization and chloritization processes lead to the complete transformation into illite and/or chlorite depending on the chemistry of fluids and enclosed rocks, in particular the availability of K and Mg (Chamley, 1989; Lanson et al., 2009; Warr, 2022). The presence of kaolinite from the middle part of the section (ca. 3000–3600 mbsf) to the top can still represent a remnant of a detrital component, as kaolinite is often more resistant and preserved in diagenetically affected sediment deposits under 120–140 °C (Chamley, 1989; Lanson et al., 2002; Warr, 2022). The smectite peak at the very bottom of the section (ca. 4180 mbsf) is highly unusual at such depths. In this case, this peak is rather related to interlayered chlorite-smectite (i.e., corrensite). The presence of corrensite has been reported in metabasalts and related to hydrothermal environments (Bettison-Varga, 1997; Inoue and Utada, 1991), which would be consistent in this case as the sediments at the bottom of the section are in contact with the basaltic basement that due to the depth and temperature could have undergone low-degree metamorphism.

The TEM images across the section support this interpretation (Fig. 4). Clay mineral textures in the upper part of the section (Campanian-Ypresian; 2650–2100 mbsf) indicate a rather detrital origin (Fig. 4D). The flake-shaped textures on smectite particles, and the polygonal shaped texture of illite and chlorite are indicative of detrital origin (Chamley, 1989; Clauer, 1990; Fagel et al., 2001). Below this upper part (2650 mbsf; Campanian), the progressive appearance of Illite-Smectite (R1) particles with fibrous textures is already indicative of illitization, consistent with burial diagenetic processes (Bauluz et al., 2012; Lanson et al., 2009; Pearson and Small, 1988). Such textures become more prominent with depth, as interlayered particles become

smaller, thinner, and occur as elongated fibres (i.e., 'hairy-like' textures — Fig. 4B-C), which is commonly observed in diagenetic affected sequences (Lanson et al., 2009; Nadeau et al., 1985). A semi-quantitative approach to interpret these clay mineral textures is the calculation of the Kübler or 'crystallinity' index on illite-smectite interstratified clay particles at the 10-Å X-ray diffraction peak. High crystallinity (i.e., low FWHM — Full Width at Half-Maximum height) is associated with clays recrystallised during diagenesis, whereas lower crystallinity (i.e., high FWHM) is associated with detrital non-altered clay particles (Kübler and Jaboyedoff, 2000; Jaboyedoff et al., 2001). This index shows the progressive effect of diagenesis between 2500 and 3800 mbsf, with a progressive increase in crystallinity along this interval of the section (FS2). The section above 2500 mbsf shows a shift to lower FWHM values, these values are associated with the absence of illite-smectite interstratified clay particles, which is also observed in the clay mineralogy with a significant increase in the smectite content above 2500 mbsf (Fig. 2). This level appears to represent the threshold between the pristine detrital clay particles and the clay minerals altered by burial diagenesis processes. Similarly, the values around 0.4 observed below 3800 mbsf (FS2) seem to be linked to a change in lithology in the borehole, shifting from claystones to more silty-sandy sediments. Therefore, illite-smectite interstratified clay particles are rather absent in this interval and their crystallinity cannot be assessed. REE concentrations can also offer insights into the origin of clay minerals (Abbott et al., 2019; Bayon et al., 2023; Cullers et al., 1975). Excluding the Eu/Eu* anomalies as they are likely related to undercorrected high Ba contents in the samples (Fig. 3; See section 4.3 — Major and REE elements) (e.g., Lidman et al., 2019; Zhu and Itoh, 2021), the REE exhibit predominantly flat patterns, which are commonly observed in detrital clays (Fagel et al., 1992; Zhao et al., 2021). Although there is some variability within the REE patterns, with part of the samples showing a slight depletion in LREE, these patterns resemble those observed in clay particles derived from large river basins (Bayon et al., 2016). More importantly, the REE patterns do not display any Ce anomalies accompanied by marked enrichments in HREE characteristic of seawater patterns, thus suggesting that authigenic imprints during the early diagenesis stages are mostly absent (Nozaki, 2001; Zhao et al., 2021). The burial diagenetic imprint observed on clay minerals does not appear either to have impacted the REE concentrations. The clay mineral assemblages affected by burial diagenesis from below the middle part of the section (2700 mbsf; Santonian) display in fact the most typical shale-like flat patterns (Fig. 3).

The clay mineralogy, the clay particle textures, and the Kübler index indicate clearly that the clay minerals assemblages, at least between 2500 and 3800 mbsf, have been modified by burial diagenesis, although REE patterns seem to be unaffected. This interval within the borehole corresponds to most of the late Cretaceous section, and therefore the changes in clay mineralogy from borehole O-A1 cannot be interpreted in terms of changes in continental denudation processes along the South African Plateau.

5.2. Sediment provenance

Sediment provenance in ancient environments has been largely assessed through neodymium isotopes (e.g., Goldstein et al., 1984; Hindshaw et al., 2018; Peucker-Ehrenbrink et al., 2010). This isotopic system is particularly suited for provenance studies because it is relatively unaffected by weathering processes (Goldstein and Jacobsen, 1988; Hindshaw et al., 2018; McCulloch and Wasserburg, 1978) and as Nd is a quite immobile element, it is resistant to diagenetic effects (e.g., Chakrabarti et al., 2007; Clauer and Chaudhuri, 1995). This is also supported by the absence of correlation between $\varepsilon_{Nd}(t)$ and the Kübler Index (FS3), suggesting that burial diagenesis did not affect the evolution of ε_{Nd} values at this site.

The $\varepsilon_{Nd}(80)$ values from site O-A1 are relatively stable around −8.5 ε-units throughout the studied interval, except for a radiogenic excursion encompassing the Cenomanian to Coniacian interval where values reach about −7 ε-units. The recorded clay $\varepsilon_{Nd}(80)$ values are compatible with a mixed contribution of different sediment sources located on the western-central areas of the South African Plateau (Fig. 5; Gaitan et al., 2023). The increase from −8.6 to −7.1 in clay $\varepsilon_{Nd}(80)$ values between the Cenomanian to Coniacian interval (ca. 97–87 Ma) points to an increase in sediment input from rather radiogenic sources (Fig. 6). Such contribution could have come from the Saldania Belt located in the southwestern African margin (Chemale et al., 2011; mean $\varepsilon_{Nd}(80) = -6$; Supplementary table S6) or the Karoo basalts (Hawkesworth et al., 1984; mean $\varepsilon_{Nd}(80) = -4.8$; Supplementary table S6). A concomitant increase in P_2O_5 wt% and clay $\varepsilon_{Nd}(80)$ values during the Cenomanian to Coniacian interval tends to support contributions from the Karoo basalts rather than the Saldania Belt (Fig. 6). P_2O_5 wt% content is typically high (> 0.4 wt%) in volcanic rocks, including Continental Flood Basalts (CFB) like the Karoo basalts (e.g., Carlson, 1991; Jourdan et al., 2007). This interpretation is consistent with previous works based on thermochronometry of kimberlites reporting an episode of enhanced Karoo basalt erosion in the 110–90 Ma interval (Stanley et al., 2015). From the Coniacian onwards, the clay $\varepsilon_{Nd}(80)$ values decrease, reaching values around −8.5 in the Campanian (ca. 80 Ma), and remaining stable up to the Ypresian (Fig. 6). These more negative values indicate increased contributions from more nonradiogenic units (i.e., lower ε_{Nd} values), such as the Namaqua Belt (Reid, 1997; mean $\varepsilon_{Nd}(80) = -15.7$; Supplementary table S6), the Cape Belt (Dia et al., 1990; mean $\varepsilon_{Nd}(80) = -10$; Supplementary table S6) or the Karoo sediments (Dia et al., 1990; mean $\varepsilon_{Nd}(80) = -8.9$; Supplementary table S6), all located at southwestern – central areas of the South African Plateau (Fig. 5). Given the nature of these units which include very heterogeneous lithologies, further analyses including trace elements and other isotopic systems will be required to better constrain their relative contribution to the sediment sources at site O-A1. Importantly, the geological units composing the South African Plateau, that provided the sediments deposited in the Cape Basin, are largely composed of various metamorphic rocks and crystalline basement (Gaitan et al., 2023). A large area was likely covered by Karoo basalts during the late Cretaceous, and partly eroded during this interval (Stanley et al., 2015), exposing underlying Permian and Triassic sediments to erosion. Although it cannot be excluded that some clays reworked from these sediments contributed to the overall clay budget at site O-A1, we argue here that this part would have been limited compared to the clays formed in soil by weathering of the largely dominating metamorphic and crystalline basement. This is supported by the dominance of smectites in the upper part of the section not affected by diagenetic burial. Smectites are very sensitive to diagenesis and is unlikely to be inherited from ancient metamorphosed or ancient sedimentary rocks (Permian or Triassic).

The changes in contribution from the sediment sources presented here can be partially associated with the tectonic uplift experienced by the South African Plateau throughout the late Cretaceous. The initial phase of the uplift (ca. 93–80 Ma) appears to have modified the sediment sources, while the latter phase (ca. 80–70 Ma) only the sediment distribution along the western South African Basins.

The tectonic uplift of the Plateau involves a margin tilting, with a first uplift phase (ca. 93–80 Ma) affecting predominantly the eastern margin and tilting the African plateau toward the west, followed by a second phase (ca. 80–70 Ma) affecting predominantly the western margin and tilting the African plateau toward the east (Baby et al., 2019; Baby et al., 2018a; Braun et al., 2014; Stanley et al., 2021). This tilting has been inferred based on changes in sedimentation rates from the basins adjacent to the South African margin (Baby et al., 2019, Baby et al., 2018a; Braun et al., 2014; Stanley et al., 2021). Although the onset of the first uplift stage is set around 93 Ma (Baby et al., 2019, Baby et al., 2018a; Braun et al., 2014; Stanley et al., 2021), thermochronological data reports erosional cooling as early as 100 Ma (e.g., Flowers and Schoene, 2010; Stanley et al., 2013; Wildman et al., 2015). This eastern margin uplift could have brought sediments from central areas of the Plateau to the Cape Basin, which could be consistent with the increased

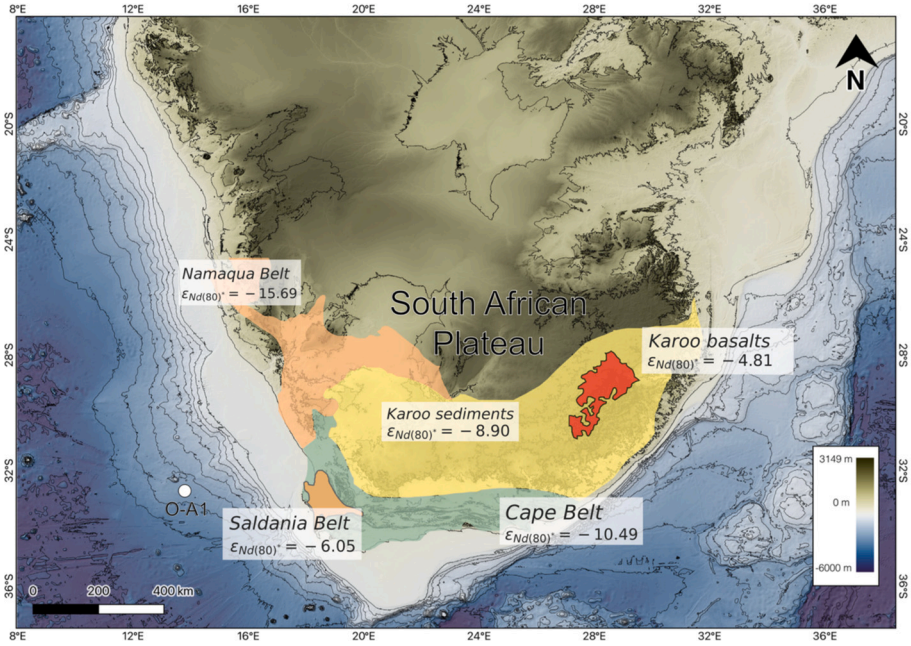

Fig. 5. Lithological units from the South African Plateau. The ε_{Nd} data compilation are as follow: 1) Karoo Basalts (Hawkesworth et al., 1984) 2) Cape Belt and Karoo Sediments (Dia et al., 1990) 3) Namaqua Belt (Reid, 1997) 4) Saldania Belt (Chemale et al., 2011). Modified after Gaitan et al. (2023).

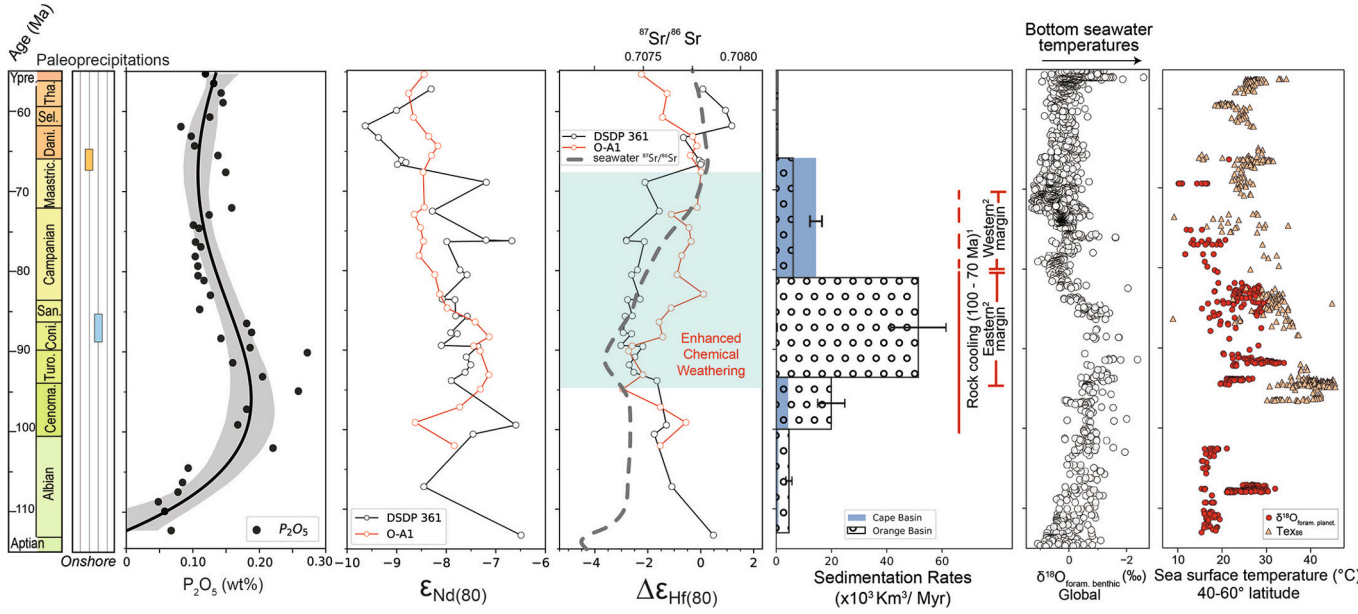

Fig. 6. P_2O_5 wt%, $\varepsilon_{Nd}(80)$ and $\Delta\varepsilon_{Hf}(80)$ values for borehole O-A1 (continental slope), $\varepsilon_{Nd}(80)$ and $\Delta\varepsilon_{Hf}(80)$ values are also reported for the DSDP 361 core (abyssal plain; Gaitan et al., 2023). Values were calculated at $t = 80$ Ma. $^{87}Sr/^{86}Sr$ ratios from McArthur et al. (2020). Palaeoprecipitations of the South African plateau are based on flora data set (Rayner et al., 1997; Sandersen, 2006; Smith, 1986). Sedimentation rates of the Cape and Orange Basins are estimations done by Baby et al. (2019). $\delta^{18}O$ records from global benthic foraminifera (black circles) are compiled from Friedrich et al. (2012); including data from Zachos et al. (2008) for the Cenozoic. Sea Surface Temperatures (SST °C) have been calculated from planktonic foraminifera $\delta^{18}O$ and Tex_{86} data reported in the PhanSST database (Judd et al., 2024) for paleolatitudes of 40–60° and excluding data with a questionable preservation indicated in the DiagenesisFlag of the database. The equation of Erez and Luz (1983) with a $\delta^{18}O_{seawater}$ of 0‰ has been used for SST from planktonic foraminifera $\delta^{18}O$, and using the linear Tex_{86}-SST calibration designed for application in warm Cretaceous climate (eq. (4) of O'Brien et al., 2017). Sample O-A1/37 was the only sample with a replicate for both the ε_{Nd} and $\Delta\varepsilon_{Hf}$ values, the values were averaged, and the mean was used for the plots. A smoothed curve and its 95% confidence interval were calculated for the P_2O_5 wt% using Kernel regressions 1) Rock cooling interval based on multiple AFT and AHe thermochronology data across the South African Plateau (Brown et al., 2002; Gallagher and Brown, 1999; Green et al., 2017; Kounov et al., 2009, 2013; Raab et al., 2002; Stanley et al., 2013, 2015, 2015; Stanley and Flowers, 2020; Tinker et al., 2008; Wildman et al., 2015, 2016) 2) Timing of the South African Plateau margins uplift is based on the erosion-deposition model proposed by Baby et al. (2019). (For interpretation of the references to colour in this figure legend, the reader is referred to the web version of this article.)

input of radiogenic sediments derived from the Karoo basalts. The switch to more nonradiogenic clay $\varepsilon_{Nd}(80)$ values after the Coniacian (ca. 87 Ma) could be related to a decrease in the contribution of radiogenic Karoo basalts that could have been partly eroded by then (Stanley

et al., 2015) or to an increased input of sediments from nonradiogenic units (e.g., Namaqua, Karoo sediments or Cape Belt), which could have been progressively incorporated during the later initial part of this first tectonic uplift stage (ca. 93–80 Ma; Fig. 6). During the second uplift stage (ca. 80–70 Ma), affecting the western margin, sediment redistribution occurred, highlighted by a decrease in sedimentation rates in the Orange basin and a concomitant increase in the Cape Basin (Fig. 6). This change could have resulted from modifications of drainage patterns, leading eventually to the merging of the Kalahari and Karoo paleorivers into the modern Orange river system that is thought to have occurred during the Maastrichtian (De Wit et al., 2009; De Wit, 1999; Goudie, 2005). Unlike the first uplift stage, this second uplift stage (ca. 80–70 Ma) does not seem to have had a major impact in the sediment sources contribution to the Cape Basin, as by the Campanian (ca. 80 Ma), the $\varepsilon_{Nd}(80)$ values have already stabilised and remained quite stable up to the Ypresian (Fig. 6).

5.3. Evolution of silicate chemical weathering in the southwestern African margin

The evolution of silicate chemical weathering is often investigated using major element ratios and indices (e.g., Baiyegunhi et al., 2017; Dinis et al., 2020). Among these indices the most commonly used is the CIA index (Chemical Index of Alteration; Nesbitt and Young, 1982). However, at site O-A1, the impact of burial diagenesis across the section could have perturbed the major elements used in this index, especially as Na and K are very mobile elements and could have been impacted by illitization processes. In addition, this index is sensitive to sediment sorting and changes in sediment sources, which vary at this site as indicated by changes in lithology and in clay $\varepsilon_{Nd}(80)$ values. Hence, the use of the CIA is not adequate for site O-A1. To investigate the evolution of silicate chemical weathering intensity, we employed the combined Sm-Nd and Lu-Hf isotopic systems from clay fractions, which have already been used in both modern and ancient environments and have shown to be independent to changes in sediment sources (e.g., Bayon et al., 2022, Bayon et al., 2016; Corentin et al., 2022). Additionally, the clay ε_{Nd} and ε_{Hf} values show no correlation with the Kübler index (FS3), suggesting that the burial diagenetic processes identified in this site did not affect the clay isotopic compositions.

During magmatic processes, the Sm-Nd and Lu-Hf isotope systems behave alike, with mantellic material enriched in Sm and Lu, leading with time to more radiogenic ε_{Nd} and ε_{Hf} values in mantellic material when compared to crustal material. This is highlighted by the correlation of crustal and mantellic ε_{Nd} and ε_{Hf} material, called the "Terrestrial Array" (Vervoort et al., 2011). Conversely, during surface continental processes these isotope systems behave differently, leading to a decoupling between ε_{Nd} and ε_{Hf} in weathering products. Autogenic processes within sediment transport such as mineral sorting are partly responsible for this decoupling, mainly due to the control exerted by zircon over ε_{Hf} values, as zircon is characterized by high concentrations and highly nonradiogenic Hf values (Bayon et al., 2006; Carpentier et al., 2014; Patchett et al., 1984). In consequence, the clay fraction — usually devoid of zircons in comparison to coarser fractions — displays higher ε_{Hf} values (Carpentier et al., 2014; Chauvel et al., 2014; Garçon et al., 2013). The clay fraction of sediments display a distinct correlation between ε_{Nd} and ε_{Hf} values denominated the "Clay Array" (Bayon et al., 2016). Within the clay fraction, it has been shown that the offset in ε_{Hf} values from the clay array, expressed as $\Delta\varepsilon_{Hf}$, is dependent on silicate weathering intensity (Bayon et al., 2016). Enhanced weathering would tend to augment the release of radiogenic Hf from easy weatherable and Lu-enriched mineral phases (Bayon et al., 2006) into the solutes from which clay minerals precipitate, therefore they exhibit an increase in their ε_{Hf} values.

While zircons are typically present in trace amounts within clay fractions, if they are present in substantial quantities they can have an impact on the evolution of ε_{Hf} on clay fractions. In our study, Zr concentrations of the analysed samples oscillate between 120 and 180 ppm (Supplementary table S2), which falls within the range of the zircon-poor clay fraction and thus discards any significative influence of zircons in our ε_{Hf} values (Bayon et al., 2016; Corentin et al., 2022). Most importantly, there is no correlation between Zr concentrations and the $\Delta\varepsilon_{Hf}$ and ε_{Hf} values (FS4), indicating that changes in $\Delta\varepsilon_{Hf}$ are not controlled by zircon abundance, but can be attributed mainly to changes in silicate chemical weathering intensity.

Following Eq. 1, $\Delta\varepsilon_{Hf}(80)$ values were calculated to assess changes in silicate chemical weathering intensity. As for ε_{Nd} values, an age correction of $t = 80$ Ma has been uniformly applied to the ε_{Hf} values to calculate the $\Delta\varepsilon_{Hf}(80)$ (Table 1). This correction corresponds to the average age of the analysed time interval. Based on Bayon et al. (2016), the increase in $\Delta\varepsilon_{Hf}(80)$ values observed from the Turonian to the Maastrichtian (ca. 95–68 Ma; Fig. 6) points to a long-term enhancement of silicate chemical weathering intensity in the South African Plateau, that only decreases after the Cretaceous-Paleogene (K-Pg) boundary. The initial increase in $\Delta\varepsilon_{Hf}(80)$ values between the Turonian and the Coniacian is concomitant to the suggested weathering of the Karoo basalts, as previously shown by $\varepsilon_{Nd}(80)$ values and P_2O_5 wt%. However, while there is a shift to more nonradiogenic $\varepsilon_{Nd}(80)$ values around the Coniacian (ca. 87 Ma), indicating the input of a different sediment source, the $\Delta\varepsilon_{Hf}(80)$ still shows a continuing increase in the intensity of silicate chemical weathering that extends up to the Maastrichtian. Therefore, if weathering of fresh, easily weatherable basaltic material could have participated at first to intensify silicate weathering on the continent, an other driver is needed to explain the continuing increase in $\Delta\varepsilon_{Hf}$ until the Maastrichtian that is not related to a change in sediment sources.

The new combined ε_{Nd} and ε_{Hf} data from site O-A1 support the intensification of silicate chemical weathering processes in the South African Plateau during the late Cretaceous, which has been depicted at the more distal site DSDP 361 (Gaitan et al., 2024). Both sites display mostly concordant sediment sources as suggested by the $\varepsilon_{Nd}(80)$ values (Fig. 6). However, the geochemical signals recorded at both sites display differences in their evolution. While records from borehole O-A1 show an enhancement in silicate chemical weathering through an increase in $\Delta\varepsilon_{Hf}(80)$ values between the Cenomanian to the Maastrichtian (Fig. 6), records from DSDP core 361 show an increase from the Campanian to the Danian. Part of this discrepancy can be related to the uncertainties in the age model from DSDP core 361, which are more pronounced for the Turonian-Santonian interval (Gaitan et al., 2023). However, during the Maastrichtian-Danian interval where the age model is better calibrated for both sites their $\Delta\varepsilon_{Hf}(80)$ records clearly differ. These differences in the isotopic record during the K-Pg transition could be related to the input of different source material into the abyssal plain where the DSDP core 361 is located, which would explain differences in $\varepsilon_{Nd}(80)$ values between the two sites at that time.

5.4. Insights on climate, erosion, and weathering

Clay mineralogy is commonly used to assess the relative evolution of physical erosion (e.g., Corentin et al., 2022, 2023; John et al., 2012), however, the clay mineralogy from site O-A1 cannot be used. The clay assemblages have been clearly affected by burial diagenetic processes at least below 2500 mbsf (ca. 66 Ma), thus their content is not indicative of surface continental processes below this depth. Published clay mineral assemblages reported for the abyssal plain of the Cape Basin (i.e., DSDP 361) show an increase in illite and chlorite over smectite during the Campanian-Danian interval (Gaitan et al., 2023). This increase in primary clays over secondary clays has been interpreted as a relative increase in physical erosion processes, and it is coherent with existing thermochronological analyses across the South African Plateau that have constrained rock cooling episodes interpreted as enhanced denudation during the mid-late Cretaceous (Brown et al., 2002; Gallagher and Brown, 1999; Green et al., 2017; Kounov et al., 2009, 2013; Stanley

et al., 2013, 2015; Stanley and Flowers, 2020; Tinker et al., 2008; Wildman et al., 2015, 2016). The onset of these cooling episodes around the margins — interpreted primarily as erosional cooling — are dated around 100 Ma and extending up to 70 Ma (Brown et al., 2002; Gallagher and Brown, 1999; Green et al., 2017; Kounov et al., 2009, 2013; Tinker et al., 2008; Wildman et al., 2015, 2016). Additional AHe data (Apatite-Helium) from inner areas of the Plateau have also shown an eastern erosional wave between ca. 120 and 60 Ma (Stanley et al., 2015; Stanley et al., 2013; Stanley and Flowers, 2020).

These rock cooling episodes have been used to link tectonic uplift with enhanced physical erosion and increases in sedimentation rates along the South African margin during the late Cretaceous (Baby et al., 2019, 2018a; Braun et al., 2014; Stanley et al., 2021). The data point to a relatively large interval of rock cooling (100-70 Ma), with sedimentation rates showing a climax in the Turonian-earliest Campanian interval (93.5 to 81 Ma; Baby et al., 2019). Considering the age uncertainties and resolution of these thermochronological and sedimentary data, this overall interval of high denudation may reflect a single uplift event as well as multiple exhumation episodes within this interval. This period also corresponds to the main increase in $\Delta\varepsilon_{Hf}(80)$ associated with enhanced weathering of the margin, suggesting that the tectonic uplift of the South African Plateau and associated increase in denudation rates during the late Cretaceous resulted in an enhancement of chemical weathering intensity.

The increase in silicate chemical weathering intensity recorded by $\Delta\varepsilon_{Hf}(80)$ data starting from the Turonian onward slightly predates the onset of the global climatic cooling recorded during the late Cretaceous (Friedrich et al., 2012; O'Brien et al., 2017; Huber et al., 2018). Sea-surface temperatures at all latitudes inferred from Tex_{86} and planktonic foraminifera $\delta^{18}O$ as well as global deep-sea temperatures from benthic foraminifera $\delta^{18}O$ record a cooling starting after the Turonian. The exact timing of the cooling onset appears to differ depending on localities (Petrizzo et al., 2022), within the end-Turonian to the earliest Campanian interval, but compilations highlight a phase of more pronounced cooling in the Santonian to Early Campanian interval (Friedrich et al., 2012; O'Brien et al., 2017; Huber et al., 2018; Petrizzo et al., 2022; Judd et al., 2024). If the initial increase in silicate chemical weathering intensity may have been favoured by the persistence of a hot greenhouse climate up to part of the Coniacian, from the Santonian onward $\Delta\varepsilon_{Hf}(80)$ values remain stable or slightly increase to reach their highest values in the Maastrichtian (Fig. 6). This long-term increase from the Turonian to the Maastrichtian (ca. about 90 to 70 Ma) persisting even during cooling climate conditions hints to the predominance of tectonic over climate as the main driver of weathering processes in the studied region, as these later cooler conditions tend to hamper the kinetics of silicate chemical weathering reactions (Maher, 2010; Riebe et al., 2004).

Interestingly, the global seawater $^{87}Sr/^{86}Sr$ records a concomitant increase from the Turonian to the Maastrichtian (Fig. 6; McArthur et al., 2020). The strontium isotopic composition of seawater is controlled by continental Sr fluxes linked to chemical weathering rates and isotopic composition of weathered material, and by mantle input from ridge spreading. A reduction in oceanic crust production (Van Der Meer et al., 2014) could have partly contributed to raise the seawater $^{87}Sr/^{86}Sr$ ratio during the late Cretaceous. Yet the striking temporal correspondence of increasing $^{87}Sr/^{86}Sr$ with enhanced weathering intensity depicted by $\Delta\varepsilon_{Hf}(80)$ and enhanced denudation of the south-eastern African margin hints to a possibly increasing contribution to seawater of continental Sr weathered from the South African continent. If this hypothesis is confirmed, it would imply a concomitant increase of denudation, weathering rates, and weathering intensity of the southwestern African margin during the late Cretaceous.

The increase in $\Delta\varepsilon_{Hf}(80)$ in site O-A1 slightly precedes an increase in Ba (ppm) and CaO wt% during the Santonian-Maastrichtian interval (ca. 85–65 Ma) suggesting also a local increase in marine productivity (Fig. 7A). The increase in CaO wt% can be initially linked to carbonate productivity, especially due to the presence of the planktonic foraminifera used to establish the age model of the site. However, to determine whether this increase is associated with marine productivity or to a detrital input, the fraction of Ba can be normalized to Al to determine the biogenic component of Ba (Baxs), which can be used as a proxy to determine export production (i.e., carbon flux to the deep ocean) (Bridgestock et al., 2019; Dymond et al., 1992; Eagle et al., 2003; Liu et al., 2018; Paytan and Griffith, 2007). The evolution of Baxs shows indeed an increase during the Santonian-Maastrichtian interval, but more importantly appears to show a positive correlation with $\Delta\varepsilon_{Hf}(80)$ (Fig. 7B). This link suggests that enhanced chemical weathering, favouring phosphorus release either from apatite in magmatic rocks or

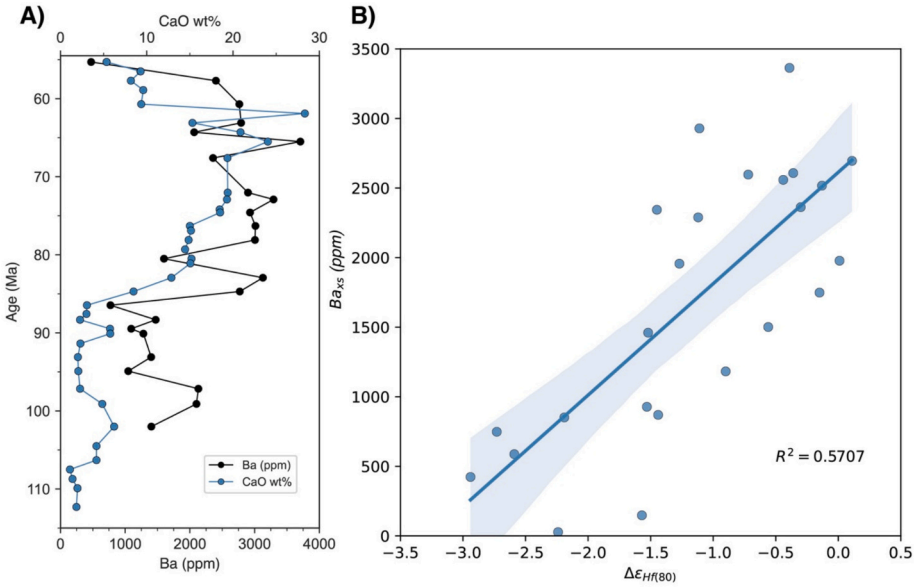

Fig. 7. A) Evolution of Ba (ppm) and CaO wt% along the borehole O-A1. B) Linear correlation and its 95% confidence interval between Ba_{xs} and $\Delta\varepsilon_{Hf}(80)$. Ba_{xs} was calculated as: $Ba_{xs} = Ba_{total} - \left(\frac{Ba}{Al}\right)_{ter} \times Al_{total}$. $(Ba/Al)_{ter}$ ratio value used for the calculations was 0.0075, which reflects the average upper crust (Dymond et al., 1992).

from apatite or secondary phosphate-bearing minerals in continental soils (Banfield and Eggleton, 1989; Chen et al., 2023), could represent a source of nutrients promoting and sustaining high productivity in this setting (e.g., Pogge von Strandmann et al., 2013; Yobo et al., 2021; Guo et al., 2024). The correlation between increases in silicate chemical weathering intensity (based on $\Delta\varepsilon_{Hfclays}$) and nutrient export production, has already been proposed as a mechanism by which silicate chemical weathering can also impact atmospheric CO_2 levels. This mechanism occurs through enhanced organic carbon burial driven by increased nutrient release, in addition to the CO_2 drawdown from silicate weathering reactions (e.g., Chen et al., 2023; Bayon et al., 2024). Analyses such as TOC (total organic content), $\delta^{13}C$, or organic phosphorus, are however required to get independent insights on the potential evolution of export production (Schoepfer et al., 2015).

Our new data from site O-A1 reveals an onset of enhanced silicate chemical weathering intensity, which may have been accompanied by an increase in chemical weathering rates suggested by seawater $^{87}Sr/^{86}Sr$ as early as the Turonian (Fig. 6), thus preceding the onset of the late Cretaceous cooling (Friedrich et al., 2012; O'Brien et al., 2017; Huber et al., 2018; Petrizzo et al., 2022). This evolution could also have potentially contributed to promote and sustain primary productivity between the Santonian and the Maastrichtian (Fig. 7). This suggests, for the first time, that the increase in silicate chemical weathering intensity and possibly rate across the South African Plateau could have contributed as one of the triggering factors in the atmospheric CO_2 drawdown and subsequent onset of the global cooling trend during the late Cretaceous. First, through atmospheric CO_2 drawdown by silicate weathering reactions, and later in the Santonian - Maastrichtian by potentially enhancing primary productivity and organic carbon storage sustained by enhanced nutrient supply from the South African Plateau.

Importantly, weathering intensity alone does not provide constraints on absolute quantities of carbon involved in biogeochemical reactions during continental weathering, that requires quantification of weathering rates and fluxes. In addition, although our new data point to a potentially important role of southern Africa uplift in triggering and sustaining the late Cretaceous cooling, enhanced weathering of other parts of the world have likely contributed as well. Relief formation has been reported around the Tethys linked to the convergence of Africa and Eurasia at that time (Chenot et al., 2018, 2021). Tectonic uplifts have also been reported on the western African and eastern South American margins based of $\Delta\varepsilon_{Hf}$ records although starting later in the late Cretaceous, as the response of chemical weathering strongly depends on local tectonic and climatic conditions (Corentin et al., 2022, 2023, 2024). A decrease in mantle CO_2 degassing has also been suggested to partly contribute to this long-term climate cooling (Van Der Meer et al., 2014; Brune et al., 2016; Corentin et al., 2022, 2023). Coupled geochemical and climate models are now needed to quantify carbon fluxes and constrain quantitatively the impact of these processes in atmospheric CO_2 drawdown and on global climate evolution.

6. Conclusion

Our data from borehole O-A1 suggest, for the first time, that tectonically driven enhancement of silicate chemical weathering along the South African Plateau might have played a crucial role in the triggering of the late Cretaceous global cooling trend that started around the Cenomanian-Turonian transition. Additionally, the impact of enhanced silicate chemical weathering in CO_2 seems to extend beyond the silicate mineral reactions, and also could be potentially related to the enhancement of primary productivity and organic carbon storage, which is a process that also captures carbon.

Our new $\Delta\varepsilon_{Hf}(80)$ data indicate an increase in silicate chemical weathering intensity and rate from the Cenomanian up to the Maastrichtian. The early phase (i.e., Cenomanian-Coniacian) of enhanced erosion and silicate chemical weathering is linked to the denudation of the Karoo basalts. This is supported by $\varepsilon_{Nd}(80)$ and P_2O_5 wt% data, which show patterns relatable to the incorporation of sediments derived from basaltic volcanic rocks. The $\varepsilon_{Nd}(80)$ data suggest that the main sediment source of the Cape Basin are units from the western-central areas of the South African Plateau, including the Karoo basalts, Karoo sediments, and potentially the Cape, Saldania, and Namaqua belts. Yet, there are some discrepancies between the DSDP core 361 and the borehole O-A1 record. Discrepancies in the $\Delta\varepsilon_{Hf}(80)$ evolution during the Cenomanian-Santonian interval (ca. 97–83 Ma) are likely linked to age model uncertainties from the DSDP core 361. Overall, our study highlights the pertinence of extended basin analysis using multiple records across the basin to understand and interpret denudation records, and to link them with changes in response to climatic and tectonic forcings.

CRediT authorship contribution statement

Camilo E. Gaitan: Writing – review & editing, Writing – original draft, Investigation, Formal analysis, Data curation. **Emmanuelle Pucéat:** Writing – review & editing, Validation, Supervision, Resources, Funding acquisition, Conceptualization. **Pierre Pellenard:** Writing – review & editing, Validation, Methodology, Conceptualization. **Fabrice Monna:** Validation, Software, Methodology. **Germain Bayon:** Writing – review & editing, Validation, Methodology, Conceptualization. **Thierry Adatte:** Writing – review & editing, Validation, Resources, Methodology. **Cécile Robin:** Project administration, Funding acquisition, Conceptualization. **François Guillocheau:** Validation, Supervision, Funding acquisition, Conceptualization.

Declaration of competing interest

The authors declare the following financial interests/personal relationships which may be considered as potential competing interests: Camilo Esteban Gaitan Valencia reports financial support was provided by Horizon Europe and ANR RISE. If there are other authors, they declare that they have no known competing financial interests or personal relationships that could have appeared to influence the work reported in this paper.

Data availability

The authors confirm that all data necessary for supporting the scientific findings of this paper have been provided.

Acknowledgments

We thank the South African Petroleum Agency (SAPA) for providing access to the material (borehole O-A1). This project has received funding from the European Union's Horizon 2020 research and innovation program under the Marie Sklodowska-Curie grant agreement No 860383 (project S2S-FUTURE) and from the project ANR RISE (ANR-20-CE49-0014). We thank Rémi Chassagnon (Laboratory ICB, University of Burgundy) and INRAe of Dijon, Ludovic Bruneau of the Biogéosciences Laboratory and GISMO analytical Platform (University of Burgundy), Marie-Laure Rouget and Bleuenn Gueguen of the Pôle Spectrométrie Océan (Brest), Olivier Reubi of the Institut des Sciences de la Terre (ISTE-Lausanne), and Philippe Telouk of the ENS Lyon for their analytical support. We also thank three anonymous reviewers for their constructive comments on the manuscript.

Appendix A. Supplementary data

Supplementary data to this article can be found online at https://doi.org/10.1016/j.gloplacha.2026.105424.

References

Abbott, A.N., Löhr, S., Trethewy, M., 2019. Are clay minerals the primary control on the oceanic rare earth element budget? Front. Mar. Sci. 6.

Aizawa, M., Bluck, B., Cartwright, J., Milner, S., Swart, R., Ward, J., 2000. Constraints on the Geomorphological Evolution of Namibia from the Offshore Stratigraphic Record.

Baby, G., Guillocheau, F., Boulogne, C., Robin, C., Dall'Asta, M., 2018a. Uplift history of a transform continental margin revealed by the stratigraphic record: the case of the Agulhas transform margin along the Southern African Plateau. Tectonophysics 731–732, 104–130. https://doi.org/10.1016/j.tecto.2018.03.014.

Baby, G., Guillocheau, F., Morin, J., Ressouche, J., Robin, C., Broucke, O., Dall'Asta, M., 2018b. Post-rift stratigraphic evolution of the Atlantic margin of Namibia and South Africa: Implications for the vertical movements of the margin and the uplift history of the South African Plateau. Mar. Pet. Geol. 97, 169–191. https://doi.org/10.1016/j.marpetgeo.2018.06.030.

Baby, G., Guillocheau, F., Braun, J., Robin, C., Dall'Asta, M., 2019. Solid sedimentation rates history of the Southern African continental margins: implications for the uplift history of the South African Plateau. Terra Nova 32, 53–65. https://doi.org/10.1111/ter.12435.

Baiyegunhi, C., Liu, K., Gwavava, O., 2017. Geochemistry of sandstones and shales from the Ecca Group, Karoo Supergroup, in the Eastern Cape Province of South Africa: implications for provenance, weathering and tectonic setting. Open Geosci. 9, 340–360. https://doi.org/10.1515/geo-2017-0028.

Banfield, J.F., Eggleton, R.A., 1989. Apatite replacement and rare earth mobilization, fractionation, and fixation during weathering. Clay Clay Miner. 37 (2), 113–127.

Barrat, J.A., Keller, F., Amossé, J., Taylor, R.N., Nesbitt, R.W., Hirata, T., 1996. Determination of rare earth elements in sixteen silicate reference samples by icp-ms after tm addition and ion exchange separation. Geostand. Geoanalytical Res. 20, 133–139. https://doi.org/10.1111/j.1751-908X.1996.tb00177.x.

Bauluz, B., Yuste, A., Mayayo, M.J., Rodríguez-Navarro, A.B., González-López, J.M., 2012. Microtexture and genesis of clay minerals from a turbiditic sequence in a Southern Pyrenees foreland basin (Jaca basin, Eocene). Clay Miner. 47, 303–318. https://doi.org/10.1180/claymin.2012.047.3.02.

Bayon, G., German, C.R., Boella, R.M., Milton, J.A., Taylor, R.N., Nesbitt, R.W., 2002. An improved method for extracting marine sediment fractions and its application to Sr and Nd isotopic analysis. Chem. Geol. 187, 179–199. https://doi.org/10.1016/S0009-2541(01)00416-8.

Bayon, G., Vigier, N., Burton, K.W., Jean Carignan, A.B., Etoubleau, J., Chu, N.-C., 2006. The control of weathering processes on riverine and seawater hafnium isotope ratios. Geology 34, 433. https://doi.org/10.1130/G22130.1.

Bayon, G., Barrat, J., Etoubleau, J., Benoit, M., Bollinger, C., Révillon, S., 2009. Determination of rare earth elements, Sc, Y, Zr, Ba, Hf and Th in geological samples by ICP-MS after Tm addition and alkaline fusion 12. Geostand. Geoanal. 33 (1), 51–62.

Bayon, G., Skonieczny, C., Delvigne, C., Toucanne, S., Bermell, S., Ponzevera, E., André, L., 2016. Environmental Hf–Nd isotopic decoupling in World river clays. Earth Planet. Sci. Lett. 438, 25–36. https://doi.org/10.1016/j.epsl.2016.01.010.

Bayon, G., Giresse, P., Chen, H., Rouget, M.-L., Gueguen, B., Moizinho, G.R., Barrat, J.-A., Beaufort, D., 2023. The Behavior of rare Earth elements during Green Clay Authigenesis on the Congo Continental Shelf. Minerals 13, 1081. https://doi.org/10.3390/min13081081.

Bayon, G., Garzanti, E., Dinis, P., Beaufort, D., Barrat, J.-A., Germain, Y., Trinquier, A., Barbarano, M., Overare, B., Adeaga, O., Braquet, N., 2024. Contribution of Saharan dust to chemical weathering fluxes and associated phosphate release in West Africa. Earth Planet. Sci. Lett. 641, 118845. https://doi.org/10.1016/j.epsl.2024.118845.

Berner, R.A., Lasaga, A.C., Garrels, R.M., 1983. Carbonate-silicate geochemical cycle and its effect on atmospheric carbon dioxide over the past 100 million years. Am. J. Sci. U. S. 283, 7. https://doi.org/10.2475/ajs.283.7.641.

Bettison-Varga, L., 1997. The role of randomly mixed-layered chlorite/smectite in the transformation of smectite to chlorite. Clay Clay Miner. 45, 506–516. https://doi.org/10.1346/CCMN.1997.0450403.

Blichert-Toft, J., Chauvel, C., Albarède, F., 1997. Separation of Hf and Lu for high-precision isotope analysis of rock samples by magnetic sector-multiple collector ICP-MS. Contrib. Mineral. Petrol. 127, 248–260. https://doi.org/10.1007/s004100050278.

Bougeault, C., Pellenard, P., Deconinck, J.-F., Hesselbo, S.P., Dommergues, J.-L., Bruneau, L., Cocquerez, T., Laffont, R., Huret, E., Thibault, N., 2017. Climatic and palaeoceanographic changes during the Pliensbachian (early Jurassic) inferred from clay mineralogy and stable isotope (C-O) geochemistry (NW Europe). Glob. Planet. Change 149, 139–152. https://doi.org/10.1016/j.gloplacha.2017.01.005.

Bouvier, A., Vervoort, J.D., Patchett, P.J., 2008. The Lu–Hf and Sm–Nd isotopic composition of CHUR: Constraints from unequilibrated chondrites and implications for the bulk composition of terrestrial planets. Earth Planet. Sci. Lett. 273, 48–57. https://doi.org/10.1016/j.epsl.2008.06.010.

Braun, J., Guillocheau, F., Robin, C., Baby, G., Jelsma, H., 2014. Rapid erosion of the Southern African Plateau as it climbs over a mantle superswell: eroding southern african plateau. J. Geophys. Res. Solid Earth 119, 6093–6112. https://doi.org/10.1002/2014JB010998.

Bridgestock, L., Hsieh, Y.-T., Porcelli, D., Henderson, G.M., 2019. Increased export production during recovery from the Paleocene–Eocene thermal maximum constrained by sedimentary Ba isotopes. Earth Planet. Sci. Lett. 510, 53–63. https://doi.org/10.1016/j.epsl.2018.12.036.

Brown, R.W., Summerfield, M.A., Gleadow, A.J.W., 2002. Denudational history along a transect across the Drakensberg Escarpment of southern Africa derived from apatite fission track thermochronology. J. Geophys. Res. Solid Earth 107. https://doi.org/10.1029/2001JB000745. ETG 10–1-ETG 10–18.

Brune, S., Williams, S.E., Butterworth, N.P., Müller, R.D., 2016. Abrupt plate accelerations shape rifted continental margins. Nature 536 (7615), 201–204.

Carlson, R.W., 1991. Physical and chemical evidence on the cause and source characteristics of flood basalt volcanism. Aust. J. Earth Sci. 38, 525–544. https://doi.org/10.1080/08120099108727989.

Carpentier, M., Weis, D., Chauvel, C., 2014. Fractionation of Sr and Hf isotopes by mineral sorting in Cascadia Basin terrigenous sediments. Chem. Geol. 382, 67–82. https://doi.org/10.1016/j.chemgeo.2014.05.028.

Chakrabarti, R., Abanda, P.A., Hannigan, R.E., Basu, A.R., 2007. Effects of diagenesis on the Nd-isotopic composition of black shales from the 420 Ma Utica Shale Magnafacies. Chem. Geol. 244, 221–231. https://doi.org/10.1016/j.chemgeo.2007.06.017.

Chamley, H., 1989. Clay Sedimentology. Springer Science & Business Media.

Chauvel, C., Garçon, M., Bureau, S., Besnault, A., Jahn, B., Ding, Z., 2014. Constraints from loess on the Hf–Nd isotopic composition of the upper continental crust. Earth Planet. Sci. Lett. 388, 48–58. https://doi.org/10.1016/j.epsl.2013.11.045.

Chemale, F., Scheepers, R., Gresse, P.G., Van Schmus, W.R., 2011. Geochronology and sources of late Neoproterozoic to Cambrian granites of the Saldania Belt. Int. J. Earth Sci. 100, 431–444. https://doi.org/10.1007/s00531-010-0579-1.

Chen, H., Bayon, G., Xu, Z., Li, T., 2023. Hafnium isotope evidence for enhanced weatherability at high southern latitudes during Oceanic Anoxic Event 2. Earth Planet. Sci. Lett. 601, 117910. https://doi.org/10.1016/j.epsl.2022.117910.

Chenot, E., Deconinck, J.-F., Pucéat, E., Pellenard, P., Guiraud, M., Jaubert, M., Jarvis, I., Thibault, N., Cocquerez, T., Bruneau, L., Razmjooei, M.J., Boussaha, M., Richard, J., Sizun, J.-P., Stemmerik, L., 2018. Continental weathering as a driver of late cretaceous cooling: new insights from clay mineralogy of Campanian sediments from the southern Tethyan margin to the Boreal realm. Glob. Planet. Change 162, 292–312. https://doi.org/10.1016/j.gloplacha.2018.01.016.

Chenot, E., Pucéat, E., Freslon, N., Deconinck, J.F., Razmjooei, M.J., Thibault, N., 2021. Late cretaceous changes in oceanic currents and sediment sources in the eastern Tethys: insights from Nd isotopes and clay mineralogy. Global Planet. Change 198, 103353.

Clauer, N., 1990. Morphological, Chemical, and Isotopic evidence for an early Diagenetic Evolution of Detrital Smectite in Marine Sediments. Clays Clay Miner. 38, 33–46. https://doi.org/10.1346/CCMN.1990.0380105.

Clauer, N., Chaudhuri, S., 1995. Clays in Crustal Environments. Springer Berlin Heidelberg, Berlin, Heidelberg. https://doi.org/10.1007/978-3-642-79085-0.

Cohen, K.M., Finney, S.C., Gibbard, P.L., Fan, J.-X., 2013. The ICS International Chronostratigraphic Chart. Episodes J. Int. Geosci. 36, 199–204. https://doi.org/10.18814/epiiugs/2013/v36i3/002.

Collier, J.S., McDermott, C., Warner, G., Gyori, N., Schnabel, M., McDermott, K., Horn, B. W., 2017. New constraints on the age and style of continental breakup in the South Atlantic from magnetic anomaly data. Earth Planet. Sci. Lett. 477, 27–40. https://doi.org/10.1016/j.epsl.2017.08.007.

Corentin, P., Pucéat, E., Pellenard, P., Freslon, N., Guiraud, M., Blondet, J., Adatte, T., Bayon, G., 2022. Hafnium-neodymium isotope evidence for enhanced weathering and uplift-climate interactions during the late cretaceous. Chem. Geol. 591, 120724. https://doi.org/10.1016/j.chemgeo.2022.120724.

Corentin, P., Pucéat, E., Pellenard, P., Guiraud, M., Blondet, J., Bayon, G., Adatte, T., 2023. Late cretaceous evolution of chemical weathering at the northeastern south American margin inferred from mineralogy and Hf-Nd isotopes. Mar. Geol. 455, 106968. https://doi.org/10.1016/j.margeo.2022.106968.

Corentin, P., Pucéat, E., Pellenard, P., Guiraud, M., Blondet, J., Bayon, G., Adatte, T., 2024. Enhanced erosion and silicate weathering of the West African craton during the late cretaceous cooling evidenced by mineralogical and Hf-Nd isotope proxies. Mar. Geol. 476, 107374. https://doi.org/10.1016/j.margeo.2024.107374.

Cullers, R.L., Arnold, B., Lee, M., Wolf, C.W., 1975. Rare earth distintions in clay minerals and in the clay-sized fraction of the lower Permian Havensville and Eskridge shales of Kansas and Oklahoma. Geochim. Cosmochim. Acta 39, 1691–1703.

De Wit, M.C.J., Ward, J.D., Bamford, M.K., Roberts, M.J., 2009. The significance of the cretaceous diamondiferous gravel deposit at mahura muthla, northern cape province, South Africa. South Afr. J. Geol. 112, 89–108. https://doi.org/10.2113/gssajg.112.2.89.

De Wit, MichielC.J., 1999. The distribution and stratigraphy of inland alluvial diamond deposits in South Africa. Afr. Geosci. Rev. Spec. Ed. 3, 19–33.

Dera, G., Pellenard, P., Neige, P., Deconinck, J.-F., Pucéat, E., Dommergues, J.-L., 2009. Distribution of clay minerals in early Jurassic Peritethyan seas: Palaeoclimatic significance inferred from multiproxy comparisons. Palaeogeogr. Palaeoclimatol. Palaeoecol. 271, 39–51. https://doi.org/10.1016/j.palaeo.2008.09.010.

Dia, A., Allègre, C.J., Erlank, A.J., 1990. The development of continental crust through geological time: the south African case. Earth Planet. Sci. Lett. 98, 74–89. https://doi.org/10.1016/0012-821X(90)90089-G.

Dinis, P.A., Garzanti, E., Hahn, A., Vermeesch, P., Cabral-Pinto, M., 2020. Weathering indices as climate proxies. A step forward based on Congo and SW African river muds. Earth Sci. Rev. 201, 103039. https://doi.org/10.1016/j.earscirev.2019.103039.

Dudus, V., Dizon, E., Doczy, G., Meikle, G., Heath, R., Kumar, D., Cleaver, R., Barrett, A., McLellen, A., Peel, A., Gleghorn, I., 1992. Final Well Report O-A1. SOEKOR, South Africa.

Dymond, J., Suess, E., Lyle, M., 1992. Barium in Deep-Sea Sediment: a Geochemical Proxy for Paleoproductivity. Paleoceanography 7, 163–181. https://doi.org/10.1029/92PA00181.

Eagle, M., Paytan, A., Arrigo, K.R., van Dijken, G., Murray, R.W., 2003. A comparison between excess barium and barite as indicators of carbon export. Paleoceanography 18. https://doi.org/10.1029/2002PA000793.

Erez, J., Luz, B., 1983. Experimental paleotemperature equation for planktonic foraminifera. Geochim. Cosmochim. Acta 47 (6), 1025–1031.
Fagel, N., André, L., Chamley, H., Debrabant, P., Jolivet, L., 1992. Clay sedimentation in the Japan Sea since the early Miocene: influence of source-rock and hydrothermal activity. Sediment. Geol. 80, 27–40. https://doi.org/10.1016/0037-0738(92)90029-Q.
Fagel, N., Robert, C., Preda, M., Thorez, J., 2001. Smectite composition as a tracer of deep circulation: the case of the Northern North Atlantic. Mar. Geol. 172, 309–330. https://doi.org/10.1016/S0025-3227(00)00123-7.
Flowers, R.M., Schoene, B., 2010. (U-Th)/he thermochronometry constraints on unroofing of the eastern Kaapvaal craton and significance for uplift of the southern African Plateau. Geology 38, 827–830. https://doi.org/10.1130/G30980.1.
Freslon, N., Bayon, G., Birot, D., Bollinger, C., Barrat, J.A., 2011. Determination of rare earth elements and other trace elements (Y, Mn, Co, Cr) in seawater using Tm addition and Mg(OH)2 co-precipitation. Talanta 85, 582–587. https://doi.org/10.1016/j.talanta.2011.04.023.
Friedrich, O., Norris, R.D., Erbacher, J., 2012. Evolution of middle to late cretaceous oceans—a 55 m.y. record of Earth's temperature and carbon cycle. Geology 40, 107–110. https://doi.org/10.1130/G32701.1.
Gaillardet, J., Dupré, B., Louvat, P., Allègre, C.J., 1999. Global silicate weathering and CO2 consumption rates deduced from the chemistry of large rivers. Chem. Geol. 159, 3–30. https://doi.org/10.1016/S0009-2541(99)00031-5.
Gaitan, C.E., Pucéat, E., Pellenard, P., Blondet, J., Bayon, G., Adatte, T., Israel, C., Robin, C., Guillocheau, F., 2023. Late cretaceous erosion and chemical weathering record in the offshore Cape Basin: Source-to-sink system from Hf Nd isotopes and clay mineralogy. Mar. Geol. 466, 107187. https://doi.org/10.1016/j.margeo.2023.107187.
Gallagher, K., Brown, R., 1999. Denudation and uplift at passive margins: the record on the Atlantic margin of southern Africa. Philos. Trans. R. Soc. Lond. Ser. Math. Phys. Eng. Sci. 357, 835–859. https://doi.org/10.1098/rsta.1999.0354.
Garçon, M., Chauvel, C., France-Lanord, C., Huyghe, P., Lavé, J., 2013. Continental sedimentary processes decouple Nd and Hf isotopes. Geochim. Cosmochim. Acta 121, 177–195. https://doi.org/10.1016/j.gca.2013.07.027.
Gibbs, R.J., 1977. Clay mineral segregation in the marine environment. J. Sediment. Res. 47, 237–243. https://doi.org/10.1306/212F713A-2B24-11D7-8648000102C1865D.
Gladczenko, T.P., Hinz, K., Eldholm, O., Meyer, H., Neben, S., Skogseid, J., 1997. South Atlantic volcanic margins. J. Geol. Soc. London 154, 465–470. https://doi.org/10.1144/gsjgs.154.3.0465.
Goldstein, S.J., Jacobsen, S.B., 1988. Nd and Sr isotopic systematics of river water suspended material: implications for crustal evolution. Earth Planet. Sci. Lett. 87, 249–265. https://doi.org/10.1016/0012-821X(88)90013-1.
Goldstein, S.L., O'Nions, R.K., Hamilton, P.J., 1984. A Sm-Nd isotopic study of atmospheric dusts and particulates from major river systems. Earth Planet. Sci. Lett. 70, 221–236. https://doi.org/10.1016/0012-821X(84)90007-4.
Gomes, A.S., Vasconcelos, P.M., 2021. Geochronology of the Paraná-Etendeka large igneous province. Earth Sci. Rev. 220, 103716. https://doi.org/10.1016/j.earscirev.2021.103716.
Goudie, A.S., 2005. The drainage of Africa since the cretaceous. Geomorphology 67, 437–456. https://doi.org/10.1016/j.geomorph.2004.11.008.
Green, P.F., Duddy, I.R., Japsen, P., Bonow, J.M., Malan, J.A., 2017. Post-breakup burial and exhumation of the southern margin of Africa. Basin Res. 29, 96–127. https://doi.org/10.1111/bre.12167.
Guo, L.C., Xiong, S.F., Mills, B.J.W., Isson, T., Yang, S.L., Cui, J.Y., Wang, Y.D., Jiang, L., Xu, Z.F., Cai, C.F., Deng, Y.N., Wei, G.Y., Zhao, M.Y., 2024. Acceleration of phosphorus weathering under warm climates. Sci. Adv. 10 (28), eadm7773. https://doi.org/10.1126/sciadv.adm7773.
Hawkesworth, C.J., Marsh, J.S., Duncan, A.R., Erlank, A.J., Norry, M.J., 1984. The Role of Continental Lithosphere in the Generation of the Karoo Volcanic Rocks: Evidence from Combined Nd-and Sr-Isotope Studies.
Hilton, R.G., West, A.J., 2020. Mountains, erosion and the carbon cycle. Nat. Rev. Earth Environ. 1, 284–299. https://doi.org/10.1038/s43017-020-0058-6.
Hindshaw, R.S., Tosca, N.J., Piotrowski, A.M., Tipper, E.T., 2018. Clay mineralogy, strontium and neodymium isotope ratios in the sediments of two High Arctic catchments (Svalbard). Earth Surf. Dyn. 6, 141–161. https://doi.org/10.5194/esurf-6-141-2018.
Hirsch, K.K., Scheck-Wenderoth, M., van Wees, J.-D., Kuhlmann, G., Paton, D.A., 2010. Tectonic subsidence history and thermal evolution of the Orange Basin. Mar. Pet. Geol. 27, 565–584. https://doi.org/10.1016/j.marpetgeo.2009.06.009.
Huber, B.T., Hobbs, R.W., Bogus, K.A., Batenburg, S.J., Brumsack, H., Guerra R., Do Monte, Zhaokai, X., 2018. Tectonic, paleoclimate, and paleoceanographic history of high-latitude southern margins of Australia during the cretaceous. Preliminary Reports 369, 1–39.
Inoue, A., Utada, M., 1991. Smectite-to-chlorite transformation in thermally metamorphosed volcanoclastic rocks in the Kamikita area, northern Honshu, Japan. Am. Mineral. 76, 628–640.
Jaboyedoff, M., Bussy, F., Kübler, B., Thelin, P., 2001. Illite "crystallinity" revisited. Clay Clay Miner. 49 (2), 156–167.
Jochum, K.P., Weis, U., Schwager, B., Stoll, B., Wilson, S.A., Haug, G.H., Andreae, M.O., Enzweiler, J., 2016. Reference Values following ISO guidelines for frequently Requested Rock Reference Materials. Geostand. Geoanalytical Res. 40, 333–350. https://doi.org/10.1111/j.1751-908X.2015.00392.x.
John, C.M., Banerjee, N.R., Longstaffe, F.J., Sica, C., Law, K.R., Zachos, J.C., 2012. Clay assemblage and oxygen isotopic constraints on the weathering response to the Paleocene-Eocene thermal maximum, east coast of North America. Geology 40, 591–594. https://doi.org/10.1130/G32785.1.
Jourdan, F., Bertrand, H., Schärer, U., Blichert-Toft, J., Féraud, G., Kampunzu, A.B., 2007. Major and Trace Element and Sr, Nd, Hf, and Pb Isotope Compositions of the Karoo large Igneous Province, Botswana–Zimbabwe: Lithosphere vs Mantle Plume Contribution. J. Petrol. 48, 1043–1077. https://doi.org/10.1093/petrology/egm010.
Judd, E.J., Tierney, J.E., Lunt, D.J., Montañez, I.P., Huber, B.T., Wing, S.L., Valdes, P.J., 2024. A 485-million-year history of Earth's surface temperature. Science 385 (6715), eadk3705.
Jungslager, E.H.A., 1999. Petroleum habitats of the Atlantic margin of South Africa. Geol. Soc. Lond. Spec. Publ. 153, 153–168. https://doi.org/10.1144/GSL.SP.1999.153.01.10.
Ketzer, M., Morad, S., Amorosi, A., 2003. Predictive diagenetic clay-mineral distribution in siliciclastic rocks within a sequence stratigraphic framework. In: International Association of Sedimentologists Special Publications, pp. 43–61. https://doi.org/10.1002/9781444304336.ch2.
Koopmann, H., Schreckenberger, B., Franke, D., Becker, K., Schnabel, M., 2016. The late rifting phase and continental break-up of the southern South Atlantic: the mode and timing of volcanic rifting and formation of earliest oceanic crust. Geol. Soc. Lond. Spec. Publ. 420, 315–340. https://doi.org/10.1144/SP420.2.
Kounov, A., Viola, G., de Wit, M., Andreoli, M.A.G., 2009. Denudation along the Atlantic passive margin: new insights from apatite fission-track analysis on the western coast of South Africa. Geol. Soc. Lond. Spec. Publ. 324, 287–306. https://doi.org/10.1144/SP324.19.
Kounov, A., Viola, G., Dunkl, I., Frimmel, H.E., 2013. Southern African perspectives on the long-term morpho-tectonic evolution of cratonic interiors. Tectonophysics 601, 177–191. https://doi.org/10.1016/j.tecto.2013.05.009.
Kübler, B., Jaboyedoff, M., 2000. Illite crystallinity. Comptes Rendus de l'Académie des Sci.-Series IIA-Earth Planet. Sci. 331 (2), 75–89.
Lanson, B., Beaufort, D., Berger, G., Bauer, A., Cassagnabère, A., Meunier, A., 2002. Authigenic kaolin and illitic minerals during burial diagenesis of sandstones: a review. Clay Miner. 37, 1–22. https://doi.org/10.1180/0009855023710014.
Lanson, B., Sakharov, B., Claret, F., Drits, V., 2009. Diagenetic Smectite-to-Illite transition in clay-rich sediments: a Reappraisal of X-Ray Diffraction results using the multi-specimen method. Am. J. Sci. 309, 476–516. https://doi.org/10.2475/06.2009.03.
Lidman, F., Laudon, H., Taberman, I., Köhler, S., 2019. Eu anomalies in soils and soil water from a boreal hillslope transect – a tracer for Holocene lanthanide transport? Geochim. Cosmochim. Acta 267, 147–163. https://doi.org/10.1016/j.gca.2019.09.014.
Liu, K., Feng, Q., Shen, J., Khan, M., Planavsky, N.J., 2018. Increased productivity as a primary driver of marine anoxia in the lower Cambrian. Palaeogeogr. Palaeoclimatol. Palaeoecol. 491, 1–9. https://doi.org/10.1016/j.palaeo.2017.11.007.
Lugmair, G.W., Marti, K., 1977. SmNdPu timepieces in the Angra dos Reis meteorite. Earth Planet. Sci. Lett. 35, 273–284. https://doi.org/10.1016/0012-821X(77)90131-5.
Maher, K., 2010. The dependence of chemical weathering rates on fluid residence time. Earth Planet. Sci. Lett. 294, 101–110. https://doi.org/10.1016/j.epsl.2010.03.010.
McArthur, J.M., Howarth, R.J., Shields, G.A., Zhou, Y., 2020. Chapter 7 - Strontium Isotope Stratigraphy. In: Gradstein, F.M., Ogg, J.G., Schmitz, M.D., Ogg, G.M. (Eds.), Geologic Time Scale 2020. Elsevier, pp. 211–238. https://doi.org/10.1016/B978-0-12-824360-2.00007-3.
McCulloch, M.T., Wasserburg, G.J., 1978. Sm-Nd and Rb-Sr Chronology of Continental Crust Formation: Times of addition to continents of chemically fractionated mantle-derived materials are determined. Science 200, 1003–1011. https://doi.org/10.1126/science.200.4345.1003.
Moulin, M., Aslanian, D., Unternehr, P., 2010. A new starting point for the South and Equatorial Atlantic Ocean. Earth Sci. Rev. 98, 1–37. https://doi.org/10.1016/j.earscirev.2009.08.001.
Murphy, D.P., Thomas, D.J., 2013. The evolution of late cretaceous deep-ocean circulation in the Atlantic basins: Neodymium isotope evidence from South Atlantic drill sites for tectonic controls. Geochem. Geophys. Geosystems 14, 5323–5340. https://doi.org/10.1002/2013GC004889.
Nadeau, P.H., Wilson, M.J., McHardy, W.J., Tait, J.M., 1985. The conversion of smectite to illite during diagenesis: evidence from some illitic clays from bentonites and sandstones. Mineral. Mag. 49, 393–400. https://doi.org/10.1180/minmag.1985.049.352.10.
NASA JPL, 2013. NASA Shuttle Radar Topography Mission Global 30 Arc Second. https://doi.org/10.5067/MEASURES/SRTM/SRTMGL30.002.
Natland, J.H., 1978. Composition, Provenance, and Diagenesis of Cretaceous Clastic Sediments Drilled on the Atlantic Continental Rise off Southern Africa, Dsdp Site 361. (Implications for the early circulation of the south atlantic).
Nesbitt, H.W., Young, G.M., 1982. Early Proterozoic climates and plate motions inferred from major element chemistry of lutites. Nature 299, 715–717. https://doi.org/10.1038/299715a0.
Nozaki, Y., 2001. Rare Earth elements and their Isotopes in the Ocean. In: Steele, J.H. (Ed.), Encyclopedia of Ocean Sciences. Academic Press, Oxford, pp. 2354–2366. https://doi.org/10.1006/rwos.2001.0284.
O'Brien, C.L., Robinson, S.A., Pancost, R.D., Sinninghe Damsté, J.S., Schouten, S., Lunt, D.J., Alsenz, H., Bornemann, A., Bottini, C., Brassell, S.C., Farnsworth, A., Forster, A., Huber, B.T., Inglis, G.N., Jenkyns, H.C., Linnert, C., Littler, K., Markwick, P., McAnena, A., Mutterlose, J., Naafs, B.D.A., Püttmann, W., Sluijs, A., van Helmond, N.A.G.M., Vellekoop, J., Wagner, T., Wrobel, N.E., 2017. Cretaceous sea-surface temperature evolution: Constraints from TEX86 and planktonic foraminiferal oxygen isotopes. Earth Sci. Rev. 172, 224–247. https://doi.org/10.1016/j.earscirev.2017.07.012.

Patchett, P.J., White, W.M., Feldmann, H., Kielinczuk, S., Hofmann, A.W., 1984. Hafnium/rare earth element fractionation in the sedimentary system and crustal recycling into the Earth's mantle. Earth Planet. Sci. Lett. 69, 365–378. https://doi.org/10.1016/0012-821X(84)90195-X.

Paton, D.A., van der Spuy, D., di Primio, R., Horsfield, B., 2008. Tectonically induced adjustment of passive-margin accommodation space; influence on the hydrocarbon potential of the Orange Basin, South Africa. AAPG Bull. 92, 589–609. https://doi.org/10.1306/12280707023.

Paton, Douglas.A., di Primio, R., Kuhlmann, G., van der Spuy, D., Horsfield, B., 2007. Insights into the petroleum system evolution of the southern Orange Basin, South Africa. S. Afr. J. Geol. 110, 261–274. https://doi.org/10.2113/gssajg.110.2-3.261.

Paytan, A., Griffith, E.M., 2007. Marine barite: recorder of variations in ocean export productivity. Deep Sea Res. Part II Top. Stud. Oceanogr. 54, 687–705. https://doi.org/10.1016/j.dsr2.2007.01.007.

Pearson, M.J., Small, J.S., 1988. Illite-smectite diagenesis and palaeotemperatures in Northern North Sea Quaternary to Mesozoic shale sequences. Clay Miner. 23, 109–132. https://doi.org/10.1180/claymin.1988.023.2.01.

Petrizzo, M.R., MacLeod, K.G., Watkins, D.K., Wolfgring, E., Huber, B.T., 2022. Late cretaceous paleoceanographic evolution and the onset of cooling in the Santonian at southern high latitudes (IODP Site U1513, SE Indian Ocean). Paleoceanogr. Paleoclimatol. 37 (1), e2021PA004353.

Petschick, R., 2001. MacDiff Ver. 4.2. 5.

Petschick, R., Kuhn, G., Gingele, F., 1996. Clay mineral distribution in surface sediments of the South Atlantic: sources, transport, and relation to oceanography. Mar. Geol. 130, 203–229. https://doi.org/10.1016/0025-3227(95)00148-4.

Peucker-Ehrenbrink, B., Miller, M.W., Arsouze, T., Jeandel, C., 2010. Continental bedrock and riverine fluxes of strontium and neodymium isotopes to the oceans. Geochem. Geophys. Geosyst. 11. https://doi.org/10.1029/2009GC002869.

Pogge von Strandmann, P.A.E., Jenkyns, H.C., Woodfine, R.G., 2013. Lithium isotope evidence for enhanced weathering during Oceanic Anoxic Event 2. Nat. Geosci. 6, 668–672. https://doi.org/10.1038/ngeo1875.

Raab, M.J., Brown, R.W., Gallagher, K., Carter, A., Weber, K., 2002. Late cretaceous reactivation of major crustal shear zones in northern Namibia: constraints from apatite fission track analysis. Tectonophysics 349, 75–92. https://doi.org/10.1016/S0040-1951(02)00047-1.

Rabinowitz, P.D., LaBrecque, J., 1979. The Mesozoic South Atlantic Ocean and evolution of its continental margins. J. Geophys. Res. Solid Earth 84, 5973–6002. https://doi.org/10.1029/JB084iB11p05973.

Rayner, R.J., Bamford, M.K., Brothers, D.J., Dippenaar-Schoeman, A.S., McKay, I.J., Oberprieler, R.G., Watersl, S.B., 1997. Cretaceous Fossils From The Orapa Diamond Mine 11.

Reid, D.L., 1997. Sm-Nd age and REE geochemistry of Proterozoic arc-related igneous rocks in the Richtersveld subprovince, Namaqua Mobile Belt, Southern Africa. J. Afr. Earth Sci. 24, 621–633. https://doi.org/10.1016/S0899-5362(97)00084-5.

Renne, P.R., 2015. Age and duration of the Paraná-Etendeka flood basalts and related plumbing system. AGU Fall Meet. Abstracts T32D–06.

Riebe, C.S., Kirchner, J.W., Finkel, R.C., 2004. Erosional and climatic effects on long-term chemical weathering rates in granitic landscapes spanning diverse climate regimes. Earth Planet. Sci. Lett. 224, 547–562. https://doi.org/10.1016/j.epsl.2004.05.019.

Sandersen, A., 2006. A Palynological Investigation of the Offshore Cretaceous Sequence on the South-West Coast of South Africa (PhD Thesis).. Uni- versity of the Witswatersrand.

Schoepfer, S.D., Shen, J., Wei, H., Tyson, R.V., Ingall, E., Algeo, T.J., 2015. Total organic carbon, organic phosphorus, and biogenic barium fluxes as proxies for paleomarine productivity. Earth-Sci. Rev., Global Rev. Permian-Triassic Mass Extinction Subsequent Recovery: Part II 149, 23–52. https://doi.org/10.1016/j.earscirev.2014.08.017.

Séranne, M., Anka, Z., 2005. South Atlantic continental margins of Africa: a comparison of the tectonic vs climate interplay on the evolution of equatorial West Africa and SW Africa margins. J. Afr. Earth Sci. 43, 283–300. https://doi.org/10.1016/j.jafrearsci.2005.07.010.

Smith, R.M.H., 1986. Sedimentation and palaeoenvironments of late cretaceous crater-lake deposits in Bushmanland, South Africa. Sedimentology 33, 369–386. https://doi.org/10.1111/j.1365-3091.1986.tb00542.x.

Söderlund, U., Patchett, P.J., Vervoort, J.D., Isachsen, C.E., 2004. The ^{176}Lu decay constant determined by Lu–Hf and U–Pb isotope systematics of Precambrian mafic intrusions. Earth Planet. Sci. Lett. 219, 311–324. https://doi.org/10.1016/S0012-821X(04)00012-3.

Stanley, J.R., Flowers, R.M., 2020. Mesozoic denudation history of the lower Orange River and eastward migration of erosion across the southern African Plateau. Lithosphere 12, 74–87. https://doi.org/10.1130/L1121.1.

Stanley, J.R., Flowers, R.M., Bell, D.R., 2013. Kimberlite (U-Th)/he dating links surface erosion with lithospheric heating, thinning, and metasomatism in the southern African Plateau. Geology 41, 1243–1246. https://doi.org/10.1130/G34797.1.

Stanley, J.R., Flowers, R.M., Bell, D.R., 2015. Erosion patterns and mantle sources of topographic change across the southern African Plateau derived from the shallow and deep records of kimberlites. Geochem. Geophys. Geosyst. 16, 3235–3256. https://doi.org/10.1002/2015GC005969.

Stanley, J.R., Braun, J., Baby, G., Guillocheau, F., Robin, C., Flowers, R.M., Brown, R., Wildman, M., Beucher, R., 2021. Constraining plateau uplift in southern africa by combining thermochronology, sediment flux, topography, and landscape evolution modeling. J. Geophys. Res. Solid Earth 126. https://doi.org/10.1029/2020JB021243.

Stevenson, I.R., Mcmillan, I.K., 2004. Incised valley fill stratigraphy of the Upper cretaceous succession, proximal Orange basin, Atlantic margin of southern Africa. J. Geol. Soc. Lond. 185–208.

Surdam, R.C., Crossey, L.J., 1987. Integrated diagenetic modeling: a process-oriented approach for clastic systems. Annu. Rev. Earth Planet. Sci. 15, 141–170. https://doi.org/10.1146/annurev.ea.15.050187.001041.

Tanaka, T., Togashi, S., Kamioka, H., Amakawa, H., Kagami, H., Hamamoto, T., Yuhara, M., Orihashi, Y., Yoneda, S., Shimizu, H., Kunimaru, T., Takahashi, K., Yanagi, T., Nakano, T., Fujimaki, H., Shinjo, R., Asahara, Y., Tanimizu, M., Dragusanu, C., 2000. JNdi-1: a neodymium isotopic reference in consistency with LaJolla neodymium. Chem. Geol. 168, 279–281. https://doi.org/10.1016/S0009-2541(00)00198-4.

Taylor, S.R., McLennan, S.M., 1985. The Continental Crust: Its Composition and Evolution.

Tinker, J., de Wit, M., Brown, R., 2008. Mesozoic exhumation of the southern Cape, South Africa, quantified using apatite fission track thermochronology. Tectonophysics 455, 77–93. https://doi.org/10.1016/j.tecto.2007.10.009.

Torsvik, T.H., Rousse, S., Labails, C., Smethurst, M.A., 2009. A new scheme for the opening of the South Atlantic Ocean and the dissection of an Aptian salt basin. Geophys. J. Int. 177, 1315–1333. https://doi.org/10.1111/j.1365-246X.2009.04137.x.

Valicenti, V.H., Pringle, A.A., Benson, J.M., 1993. Biostratigraphic Report on Borehole O-A1. Soekor.

Van Der Meer, D.G., Zeebe, R.E., van Hinsbergen, D.J., Sluijs, A., Spakman, W., Torsvik, T.H., 2014. Plate tectonic controls on atmospheric CO_2 levels since the Triassic. Proc. Natl. Acad. Sci. 111 (12), 4380–4385.

Van Der Spuy, D., 2003. Aptian source rocks in some South African cretaceous basins. Geol. Soc. Lond. Spec. Publ. 207, 185–202. https://doi.org/10.1144/GSL.SP.2003.207.10.

Velde, B., 1995. Origin and Mineralogy of Clays: Clays and the Environment. Springer Science & Business Media.

de Vera, J., Granado, P., McClay, K., 2010. Structural evolution of the Orange Basin gravity-driven system, offshore Namibia. Mar. Pet. Geol. 27, 223–237. https://doi.org/10.1016/j.marpetgeo.2009.02.003.

Vervoort, J.D., Plank, T., Prytulak, J., 2011. The Hf–Nd isotopic composition of marine sediments. Geochim. Cosmochim. Acta 75, 5903–5926. https://doi.org/10.1016/j.gca.2011.07.046.

Warr, L.N., 2022. Earth's clay mineral inventory and its climate interaction: a quantitative assessment. Earth Sci. Rev. 234, 104198. https://doi.org/10.1016/j.earscirev.2022.104198.

Weis, D., Kieffer, B., Maerschalk, C., Pretorius, W., Barling, J., 2005. High-precision Pb-Sr-Nd-Hf isotopic characterization of USGS BHVO-1 and BHVO-2 reference materials: Pb-Sr-Nd-Hf Characterization. Geochem. Geophys. Geosyst. 6. https://doi.org/10.1029/2004GC000852.

Wildman, M., Brown, R., Watkins, R., Carter, A., Gleadow, A., Summerfield, M., 2015. Post break-up tectonic inversion across the southwestern cape of South Africa: New insights from apatite and zircon fission track thermochronometry. Tectonophysics 654, 30–55. https://doi.org/10.1016/j.tecto.2015.04.012.

Wildman, M., Brown, R., Beucher, R., Persano, C., Stuart, F., Gallagher, K., Schwanethal, J., Carter, A., 2016. The chronology and tectonic style of landscape evolution along the elevated Atlantic continental margin of South Africa resolved by joint apatite fission track and (U-Th-Sm)/he thermochronology. Tectonics 35, 511–545. https://doi.org/10.1002/2015TC004042.

Wildman, M., Gallagher, K., Chew, D., Carter, A., 2021. From sink to source: using offshore thermochronometric data to extract onshore erosion signals in Namibia. Basin Res. 33, 1580–1602. https://doi.org/10.1111/bre.12527.

Yobo, L., Brandon, A.D., Holmden, C., Lau, K.V., Eldrett, J., 2021. Changing inputs of continental and submarine weathering sources of Sr to the oceans during OAE 2. Geochim. Cosmochim. Acta 303, 205–222. https://doi.org/10.1016/j.gca.2021.03.013.

Zhao, Y., Wei, W., Li, S., Yang, T., Zhang, R., Somerville, I., Santosh, M., Wei, H., Wu, J., Yang, J., Chen, W., Tang, Z., 2021. Rare earth element geochemistry of carbonates as a proxy for deep-time environmental reconstruction. Palaeogeogr. Palaeoclimatol. Palaeoecol. 574, 110443. https://doi.org/10.1016/j.palaeo.2021.110443.

Zhu, Y., Itoh, A., 2021. Pseudo isotope dilution (PID) as an approach for correcting barium-related spectral interferences on the measurement of europium by inductively coupled plasma mass spectrometry (ICP-MS). Anal. Chim. Acta 1180, 338854. https://doi.org/10.1016/j.aca.2021.338854.